



HAL
open science

Submarine karstic springs as a source of nutrients and bioactive trace metals for the oligotrophic Northwest Mediterranean Sea

Joseph Tamborski, Pieter van Beek, Pascal Conan, Mireille Pujo-Pay, Charlène Odobel, Jean-François Ghiglione, Jean-Luc Seidel, Bruno Arfib, Marc Diego-Feliu, Jordi Garcia-Orellana, et al.

► To cite this version:

Joseph Tamborski, Pieter van Beek, Pascal Conan, Mireille Pujo-Pay, Charlène Odobel, et al.. Submarine karstic springs as a source of nutrients and bioactive trace metals for the oligotrophic Northwest Mediterranean Sea. *Science of the Total Environment*, 2020, 732, pp.139106. 10.1016/j.scitotenv.2020.139106 . hal-02891620v1

HAL Id: hal-02891620

<https://hal.science/hal-02891620v1>

Submitted on 23 Feb 2021 (v1), last revised 31 Aug 2021 (v2)

HAL is a multi-disciplinary open access archive for the deposit and dissemination of scientific research documents, whether they are published or not. The documents may come from teaching and research institutions in France or abroad, or from public or private research centers.

L'archive ouverte pluridisciplinaire **HAL**, est destinée au dépôt et à la diffusion de documents scientifiques de niveau recherche, publiés ou non, émanant des établissements d'enseignement et de recherche français ou étrangers, des laboratoires publics ou privés.

2 ***Submarine karstic springs as a source of nutrients and bioactive trace***
3 ***metals for the oligotrophic Northwest Mediterranean Sea***

4 Joseph Tamborski^{1*}, Pieter van Beek¹, Pascal Conan², Mireille Pujo-Pay², Charlene Odobel²,
5 Jean-François Ghiglione², Jean-Luc Seidel³, Bruno Arfib⁴, Marc Diego Feliu⁵, Jordi Garcia-
6 Orellana^{5,6}, Armand Szafran¹, Marc Souhaut¹

7 ¹LEGOS, Laboratoire d'Etudes en Géophysique et Océanographie Spatiales (Université de Toulouse, CNES, CNRS,
8 IRD, UPS), Observatoire Midi Pyrénées, 14 Ave Edouard Belin, 31400 Toulouse, France

9 ²LOMIC, Laboratoire d'Océanographie Microbienne, Observatoire Océanologique, Sorbonne Université, CNRS,
10 UPMC Univ Paris 06, UMR7621, 66650 Banyuls/Mer, France

11 ³HydroSciences Montpellier, UMR 5569 – UM2 – CNRS – IRD – UM1 Place Eugène Bataillon -CC MSE, 34095
12 Montpellier Cedex 5, France

13 ⁴Aix Marseille Université, CNRS, IRD, INRAE, Coll France, CEREGE, Aix-en-Provence, France

14 ⁵Institut de Ciència i Tecnologia Ambientals (ICTA-UAB), Universitat Autònoma de Barcelona, Bellaterra,
15 Catalunya, Spain

16 ⁶Department de Física, Universitat Autònoma de Barcelona, Bellaterra, Catalunya, Spain

17 *Correspondence: jtamborski@whoi.edu

18 ^Present address:

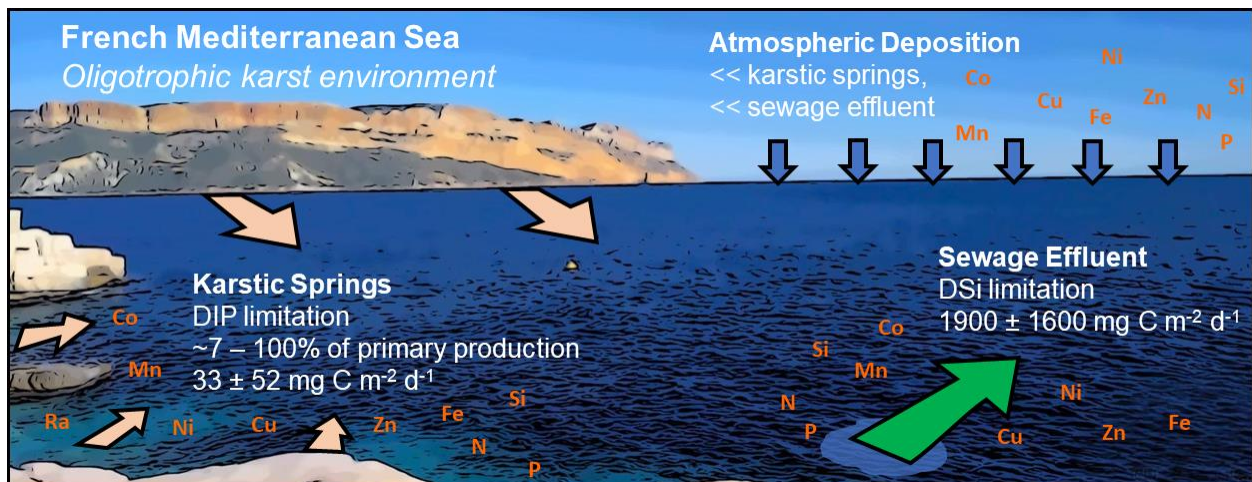
19 Department of Marine Chemistry and Geochemistry, Woods Hole Oceanographic Institution, Woods Hole, MA
20 02543 USA

21 Centre for Water Resources Studies, Dalhousie University, Halifax, NS, Canada

22 **Keywords:** karst; springs; submarine groundwater discharge; nutrients; radium isotopes; GEOTRACES

23

24 **Graphical Abstract**



25
26

27 **Abstract**

28 Groundwater springs in karstified carbonate aquifers are known to transport carbon, nutrients and trace elements to
29 the coastal ocean. The biogeochemical significance of submarine karstic springs and their impact on coastal primary
30 production are often difficult to quantify. We investigated several karstic springs, including the first-order Port-Miou
31 spring, in an urbanized watershed that is also severely impacted by sewage effluent (Calanques of Marseille-Cassis,
32 France). Karstic springs were elevated in major nutrients and bioactive trace metals over Mediterranean seawater,
33 with relatively low concentration ranges. Groundwater NO_3^- was likely derived from atmosphere-aquifer interactions,
34 while DOC:DON ratios reveal that NO_2^- and NH_4^+ was autochthonously produced during mixing between karst
35 groundwater and seawater. Submarine groundwater discharge (SGD) during March 2018 (wet season, baseflow
36 conditions) was $6.7 \pm 2.0 \text{ m}^3 \text{ s}^{-1}$ for the entire investigated coastline, determined from simultaneous ^{224}Ra and ^{226}Ra
37 mass balances. The contribution of groundwater PO_4^{3-} , the major limiting nutrient of the Mediterranean Sea, sustained
38 only 1% of primary production adjacent to sewage outfall, but between 7 and 100% of the local primary production
39 in areas that were not impacted by sewage. Groundwater and seawater Fe:DIN and Fe:DIP ratios suggest that Fe was
40 not a limiting micro-nutrient during the period of study, where bioactive trace metal fluxes were dominated by sewage
41 and atmospheric deposition, although excess Fe from groundwater may locally enhance N fixation. Groundwater
42 solute fluxes may easily vary by a factor of two or more over time because karst aquifers are sensitive to precipitation,
43 as is the case of the regional carbonate karstified aquifer of Port-Miou, highlighting the critical importance of properly
44 characterizing nutrient and trace metal inputs in these coastal environments.

45

46 **1. Introduction**

47 In coastal karstified carbonate aquifers, groundwater discharge often occurs as a point-source, in the form of
48 coastal springs and submarine springs (Fleury et al., 2007a). Karstic springs carry new carbon, nutrients, trace
49 elements, organic contaminants and even pesticides to the coastal ocean (Garcia-Solsona et al., 2010b; Gonnee et
50 al., 2014; Montiel et al., 2018; Pavlidou et al., 2014); thus, karstic springs may play a vital role in sustaining coastal
51 primary production (Lecher et al., 2018). The biogeochemical significance of karstic groundwater discharge in
52 supplying nutrients and trace metals may be particularly relevant in semi-arid regions like the oligotrophic
53 Mediterranean Sea where runoff is limited (Garcia-Solsona et al., 2010b, 2010a; Tovar-Sanchez et al., 2014; Trezzi
54 et al., 2016) and where PO_4^{3-} broadly limits primary production (Diaz et al., 2000; Krom et al., 1991). The
55 significance of karstic springs in sustaining or enhancing coastal zone primary production (Rodellas et al., 2014;
56 Tovar-Sanchez et al., 2014) has received limited attention along the French Mediterranean coastline.

57 The Ca-carbonate matrix of karstified carbonate aquifers can remove the major nutrient PO_4^{3-} from solution via
58 mineral precipitation (de Jonge and Villerius, 1989; Price et al., 2010); alternatively, carbonate mineral dissolution
59 may release adsorbed P into karst groundwaters (Pain et al., 2020). The removal of P leads to groundwaters with
60 elevated stoichiometric N:P ratios above Redfield ratio (16), which may subsequently drive the coastal ocean toward
61 P-limitation (Conan et al., 2007; Egger et al., 2015). P mineral precipitation commonly occurs in karst aquifers of
62 the Mediterranean Sea, with a median coastal groundwater N:P ratio of ~ 150 (Rodellas et al., 2015). In addition to
63 macro-nutrients, phytoplankton also require micro-nutrients for growth. Bioactive trace metals such as Cd, Mn, Fe,
64 Co, Ni, Cu and Zn play important roles in marine phytoplankton development (Morel and Price, 2003; Twining and
65 Baines, 2013), since trace metals are used as cofactors (or part of cofactors) of enzymes or as structural elements in
66 various molecules (Morel and Price, 2003). For example, Fe loading from submarine groundwater discharge (SGD)
67 has been suggested to stimulate primary production in the South Atlantic Ocean (Windom et al., 2006). Therefore,
68 concurrent evaluation of groundwater-borne nutrient and trace metal fluxes is required to properly understand the
69 impacts that karstic springs may have in sustaining or enhancing coastal zone primary production.

70 At the basin-scale, total SGD has shown to be a significant vector in transporting major nutrients (Rodellas et
71 al., 2015; Tamborski et al., 2018) and bioactive trace metals (Trezzi et al., 2016) to the oligotrophic Mediterranean
72 Sea, as compared to riverine (Pujo-Pay et al., 2006) and atmospheric inputs (Herut et al., 1999). Mediterranean karst
73 springs are significantly enriched in DIN (120 – 440 μM) and DIP (0.18 – 0.72 μM), which respectively comprise 8
74 – 31% and 1 – 4% of total riverine inputs to the entire Mediterranean Sea (Chen et al., 2020). At local-scales where
75 riverine inputs are limited, karstic springs may be even more important for coastal ecosystems. For example, karst
76 springs have been suggested to increase P-limitation along the eastern coast of Spain (Garcia-Solsona et al., 2010b)
77 and its island coves (Garcia-Solsona et al., 2010a; Tovar-Sanchez et al., 2014). Indeed, point-sourced karstic
78 groundwater nutrient loads can directly impact coastal biodiversity at the local-scale (Foley, 2018). However,
79 assessment of nutrient loads from karst aquifers is difficult to accurately constrain in space and time, in part due to
80 geologic heterogeneity and the response-time of the aquifer to precipitation (Montiel et al., 2018).

81 The Gulf of Lions, situated along the northwest Mediterranean Sea, hosts several known coastal and submarine
82 springs (Bakalowicz, 2015). Bejannin et al. (2020) recently estimated karst groundwater DSi and NO₃⁻ fluxes along
83 Côte Bleue, a region just west of the city of Marseille (eastern Gulf of Lions). In the absence of surface water inputs,
84 karst groundwater is the sole nutrient source to this region and is likely responsible for sustaining coastal zone
85 primary productivity, where karst groundwater supplies significant DSi ($6.2 \pm 5.0 \cdot 10^3 \text{ mol d}^{-1} \text{ km}^{-1}$) and NO₃⁻ +
86 NO₂⁻ ($4.0 \pm 2.0 \cdot 10^3 \text{ mol d}^{-1} \text{ km}^{-1}$) offshore. Farther east, several karstic springs are known to discharge to the
87 Calanques of Marseille-Cassis, including the springs of Sugiton, Cassis (*e.g.* the Bestouan spring) and the first-order
88 Port-Miou spring (Arfib and Charlier, 2016; Bejannin et al., 2017; Claude et al., 2019; Fleury et al., 2007a);
89 however, information on nutrient loads and estimates of primary productivity in this region are lacking.

90 Herein we provide a comprehensive analysis of the major nutrient and bioactive trace metal fluxes driven by the
91 karstic springs of the Calanques of Marseille-Cassis during baseflow conditions (*i.e.* conservative) and how these
92 karstic springs may sustain coastal zone primary production during our studied period (March 2018). This is an ideal
93 location to study because there is little to no surface water inputs; all of the runoff during precipitation events
94 infiltrates through the highly fractured limestone and dry paleo-valleys. In order to understand the role of the karstic
95 springs in coastal biogeochemical cycles, calculated chemical fluxes will be compared with sewage effluent from a
96 major urbanized Mediterranean city (Marseille) and atmospheric deposition. Thus, a major question of this research
97 is whether or not karst groundwater is relevant in sustaining primary production in metropolitan areas impacted by
98 sewage discharge. This study helps establish the significance of various nutrients and trace metals in the study area
99 and aims to elucidate the possible consequences on processes such as alterations of marine ecosystem structure and
100 function. Further, the SGD-driven chemical fluxes help to evaluate various chemical element budgets in the NW
101 Mediterranean Sea.

102 2. Materials & Methods

103 2.1 Study Site

104 The Calanques of Marseille-Cassis spans a rocky, cliff-dominated shoreline of over 20 km in length along
105 the French Mediterranean Sea (**Figure 1**). Regional precipitation is on the order of 500 – 1,000 mm a⁻¹ and primarily
106 occurs during winter, with drought-like conditions that persist during summer (Arfib and Charlier, 2016). The karst
107 Port-Miou aquifer is composed of Jurassic and Cretaceous limestone, dolostone and mixed siliciclastic-carbonate
108 rocks with a recharge area of over 400 km². The Port-Miou spring is one of the largest karstic springs in coastal
109 Europe (Custodio, 2010) and is the primary spring of this region. The primary submarine karst spring discharges at a
110 depth of ~12 m below sea level from a karstic conduit in excess of 100 m² (Fleury et al., 2007a). Karstic
111 groundwaters are brackish, reflecting a mixture between freshwater and seawater in the upstream part of the karst
112 network (Blavoux et al., 2004; Cavalera, 2007). A submarine dam was constructed in the 1970's in the main karst
113 conduit to prevent further seawater intrusion; however, groundwater salinities remain elevated due to present day
114 seawater intrusion at depth. The deep reservoir of the Port-Miou aquifer is hypothesized to have such a large mixing
115 zone and transit time that the first-magnitude spring is considered to discharge at a relatively constant salinity (~12 –
116 14 PSU) and flow-rate (~ 3 m³ s⁻¹) during baseflow conditions (*i.e.* no precipitation); in contrast, the shallow
117 reservoir of the aquifer responds rapidly to precipitation and can exceed 20 m³ s⁻¹ immediately following a rainfall-
118 event (Arfib and Charlier, 2016; Claude et al., 2019).

119 The Huveaune River (~0.3 – 65 m³ s⁻¹) and Jarret River merge in the city of Marseille (**Figure 1**), where
120 they mix with treated wastewater (~1.7 million people). The combined waters form the Cortiou sewage outfall and
121 flows to the Mediterranean Sea (Savriama et al., 2015). The wastewater treatment plant (WWTP) can handle a
122 maximum discharge between 3 and 6.5 m³ s⁻¹; the remaining flow goes untreated in the event of heavy rainfall. The
123 combined sewage and Huveaune River discharge in dry periods averages ~2.9 m³ s⁻¹ (Oursel et al., 2013). The
124 WWTP chemical loading decreased between 1984 and 1999 with the development of a primary treatment plant
125 (Bellan et al., 1999; Perez et al., 2005); however, eutrophication and adverse ecological phenomena persist in the
126 region adjacent to the sewage outfall to date.

127 2.2 Field Methods

128 Seawater samples were collected offshore of the Calanques of Marseille-Cassis on 27 – 28 March 2018
129 aboard the *R/V Antédon II* (**Figure 1**). Surface waters were collected from ~0.5 m depth using a trace-metal-clean
130 submersible pump. Coastal surface waters, waters from the outlet of the Cortiou WWTP and karstic springs were
131 sampled from a Zodiac on 28 – 29 March 2018. Four submarine karstic springs were sampled by SCUBA divers,
132 where a trace-metal-clean submersible pump was placed directly within the subterranean karst conduit. Two
133 surficial springs were sampled in Port-Miou, which were connected to the main karst conduit (**Figure 1**). Salinity
134 (PSU) and temperature were measured *in-situ* from the shipboard CTD sensor (conductivity/temperature/depth) and
135 from a handheld WTW probe (Xylem) for the coastal samples aboard the Zodiac.

136 Continuous *in-situ* salinity time-series of the Port-Miou brackish spring were recorded with a CTD Diver
137 sensor (15-minute time step; Schlumberger) at the underground dam, 500 m inland in the main flooded karst conduit
138 discharging in the Calanque of Port-Miou (Port-Miou *in-situ* observatory). *In-situ* discharge time-series of the
139 Huveaune River (**Figure 1**) was recorded at the State gauging station Aubagne-Huveaune (Banque Hydro
140 #Y4424040). Rainfall was recorded in the area that encompasses the Huveaune River watershed and the recharge
141 area of the Port-Miou and Bestouan karst springs (Arfib and Charlier, 2016) at the Aubagne State rain gauge station
142 (Météo France #13005003; **Figure 1**).

143 2.3 Analytical Methods

144 Samples for nitrate (NO_3^-), nitrite (NO_2^-), silicate ($\text{Si}(\text{OH})_4$) and phosphate (PO_4^{3-}) were prefiltered onto 25
145 mm updisc RC (~0.45 μm) PP, collected into 50 mL polyethylene flasks and stored frozen until analysis. Samples
146 for ammonium (NH_4^+) determination were collected into 60 mL polycarbonate tubes and analyzed directly in the
147 field. NO_3^- , NO_2^- , $\text{Si}(\text{OH})_4$ and PO_4^{3-} were analyzed using an automated colorimetric method (Aminot and Kerouel,
148 2007). The detection limits were 0.05 μM for NO_3^- , NO_2^- and $\text{Si}(\text{OH})_4$, and 0.02 μM for PO_4^{3-} with measurement
149 accuracies of $\pm 0.02 \mu\text{M}$, $\pm 0.02 \mu\text{M}$ and $\pm 0.005 \mu\text{M}$ and $\pm 0.005 \mu\text{M}$, respectively. NH_4^+ concentration was measured
150 by using the fluorescent procedure of Holmes et al. (1999) with a detection limit of 0.005 μM and a measurement
151 accuracy of $\pm 0.015 \mu\text{M}$. Select samples for Dissolved Organic Nitrogen (DON) and Phosphorus (DOP) were
152 prefiltered through 2 combusted (24 h, 450°C) glass fiber filters (Whatman GF/F, 25 mm), collected in Teflon vials,
153 then poisoned with HgCl_2 and stored at 4°C until analysis. In the laboratory, samples were analyzed by persulfate
154 wet-oxidation according to Pujol-Pay and Raimbault (1994) and Pujol-Pay et al. (1997). The detection limits were 0.2
155 μM for DON and 0.02 μM for DOP, with measurement accuracies of $\pm 0.3 \mu\text{M}$ for DON and $\pm 0.02 \mu\text{M}$ for DOP.

156 Samples for Dissolved Organic Carbon (DOC) were filtered through 2 pre-combusted (24 h, 450 °C) glass
157 fiber filters (Whatman GF/F, 25mm) and collected into a pre-combusted glass sealed ampoule acidified with
158 orthophosphoric acid. Samples were then analyzed by high temperature catalytic oxidation (Sugimura and Suzuki,
159 1988) on a Shimadzu TOCL analyzer. Typical analytical precision is ± 0.1 –0.5 (SD) or 0.2–1% (CV).
160 Standardization and data quality were assured through the use of consensus reference materials
161 (<http://www.rsmas.miami.edu/groups/biogeochem/CRM.html>) that was injected every 12 to 17 samples to insure
162 stable operating conditions. Particulate Organic Carbon (POC) and Nitrogen (PON) were collected on pre-
163 combusted (24 h, 450 °C) glass fiber filters (Whatman GF/F, 25mm). Filters were dried in an oven at 50 °C and
164 stored in ashed glass vials and in a desiccator until analysis on a CHN Perkin Elmer 2400.

165 For prokaryotic abundance, 1.8 mL of (select) samples were fixed with glutaraldehyde (1% final
166 concentration). Samples were incubated for 15 minutes in the dark at ambient temperature and then stored at -80°C
167 until flow cytometric analysis. A 1 mL sub-sample was incubated with SYBR Green I (Invitrogen–Molecular
168 Probes) at 0.025% (v/v) final concentration for 15 minutes at room temperature in the dark. Counts were performed
169 with a FACS Calibur flow cytometer (Becton Dickinson) equipped with an air-cooled argon laser (488 nm, 15 mW;
170 van Wambeke et al., 2009).

171 Karstic spring and (select) seawater samples for trace element determination were filtered on site with
172 disposable polypropylene syringes and Durapore membranes (0.22 μm) and stored in acid washed HDPE bottles
173 after acidification with ultrapure HNO_3 (1% v/v). Trace elements (Mn, Fe, Co, Ni, Cu and Zn) were analyzed with
174 Q-ICPMS (iCAP Q, Thermo Scientific® equipped with an Argon Gas Dilution in-line system) after acidification at
175 1% v/v HNO_3 at the AETE-ISO (Analyse des Elements en Trace dans l'Environnement et Isotopes) technical
176 platform of the OSU OREME, University of Montpellier. The Argon Gas Dilution in-line system enables the
177 introduction of highly mineralized samples without previous dilution. Instrument calibrations were carried out with
178 synthetic multi-elemental solutions. Instrumental drift was monitored and corrected by addition of a multi-elemental
179 (Be, Sc, Ge, Rh, Ir) internal standard. Reagent and procedural blanks were measured in parallel to sample treatment
180 using identical procedures. Precision error was typically < 10%. CASS-6 seawater reference material for trace
181 metals (National Research Council, Canada) was analyzed every 20 samples to check the analysis accuracy (**Table**
182 **S1**). Mean results are within the range of certified uncertainties and deviation of measured values was < 10% of
183 certified concentrations.

184 Approximately ~110 L of seawater per station was collected for Ra isotopes on board the *R/V Antédon II*
185 (offshore samples); between ~20 and 40 L of water was collected from the coastal stations. Ra isotope samples were
186 collected into plastic cubitainers, weighed and filtered through MnO_2 -coated acrylic fibers (Mn-fiber) at a flow-rate
187 of < 1 L min^{-1} to quantitatively adsorb dissolved Ra isotopes onto the Mn-fiber (Moore and Reid, 1973). The Mn-
188 fibers were triple rinsed with Ra-free deionized water and partially-dried using compressed-air until a fiber-to-water
189 ratio of 1:1 was achieved (Sun and Torgersen, 1998). The short-lived ^{223}Ra and ^{224}Ra isotopes were counted using a
190 delayed coincidence counter (RaDeCC) (Moore and Arnold, 1996) following the counting recommendations
191 described in Diego-Feliu et al. (2020). In the case of high activity samples, a second count was performed between 7

192 – 10 days after sample collection to determine the activity of ^{223}Ra . Samples were counted one month after
 193 collection to quantify ^{228}Th , in order to determine the activity of unsupported, excess ^{224}Ra (denoted $^{224}\text{Ra}_{\text{ex}}$
 194 hereafter). Detectors were calibrated from measurements of ^{232}Th standards (Moore and Cai, 2013); activities and
 195 uncertainties were calculated following Garcia-Solsona et al. (2008). Long-lived ^{226}Ra was quantified via the
 196 ingrowth of its daughter ^{222}Rn using the RaDeCC system (Geibert et al., 2013).

197 2.4 Water Flow Calculations

198 Ra isotopes were used to quantify karstic spring inputs to the coastal zone of the Calanques of Marseille-
 199 Cassis. These isotopes are typically enriched by one to three orders of magnitude in coastal groundwaters relative to
 200 seawater, making them effective tracers of SGD in karst environments (Garcia-Solsona et al., 2010a, 2010b; Tovar-
 201 Sanchez et al., 2014). Karst aquifers are typically enriched in U relative to Th, and therefore in U-series daughters
 202 (e.g. $^{226}\text{Ra} \gg ^{228}\text{Ra}$; Charette et al., 2007); we thus use ^{226}Ra , in addition to ^{224}Ra , also enriched in the spring waters,
 203 in the ensuing analysis. The coastal zone of the Calanques of Marseille-Cassis was sub-divided into five unique
 204 areas, following coastal geomorphological features (boxes 1 – 5; **Figure 1**). We note that the Calanque of Port-Miou
 205 (box 4) mixes with box 5 (Cassis); in the ensuing analysis these boxes are separated from each other across the inlet
 206 of Port-Miou (**Figure 1**).

207 Runoff in this region is insignificant and we neglect the molecular diffusion of Ra isotopes from sediments
 208 because the coastline is predominately carbonate rock (very little unconsolidated sediment; Bejannin et al., 2017). A
 209 steady-state mass balance of short-lived ^{224}Ra ($t_{1/2} = 3.66$ d) and long-lived ^{226}Ra ($t_{1/2} = 1,600$ y) was constructed for
 210 each individual box,

$$211 \frac{d^{224}\text{Ra}}{dt} = Q_{\text{WWTP}}^{224} * ^{224}\text{Ra}_{\text{WWTP}} + ^{224}\text{Ra}_{\text{SGD}} * Q_{\text{SGD}} - (^{224}\text{Ra}_{\text{box}} * V_{\text{box}} * \lambda_{224}) - (^{224}\text{Ra}_{\text{box}} - ^{224}\text{Ra}_{\text{sea}}) * \frac{V_{\text{box}}}{\tau_{\text{box}}}$$

212 (Eq. 1)

$$213 \frac{d^{226}\text{Ra}}{dt} = Q_{\text{WWTP}}^{226} * ^{226}\text{Ra}_{\text{WWTP}} + ^{226}\text{Ra}_{\text{SGD}} * Q_{\text{SGD}} - (^{226}\text{Ra}_{\text{box}} - ^{226}\text{Ra}_{\text{sea}}) * \frac{V_{\text{box}}}{\tau_{\text{box}}} \quad (\text{Eq. 2})$$

214 where Ra_{WWTP} , Ra_{SGD} , Ra_{box} and Ra_{sea} represents the mean ^{224}Ra (Eq. 1) or ^{226}Ra (Eq. 2) activity (dpm 100L⁻¹) of the
 215 wastewater treatment plant effluent, the karstic groundwater springs, the surface waters of the box under
 216 consideration and offshore Mediterranean seawater, respectively. Additional mass balance terms include the
 217 discharge of the WWTP (Q_{WWTP} ; m³ s⁻¹), submarine groundwater discharge (*i.e.* karstic spring; Q_{SGD} ; m³ s⁻¹), the
 218 volume of water within each box impacted by groundwaters (V ; m³), the ^{224}Ra decay constant ($\lambda_{224} = 0.189$ d⁻¹) and
 219 the surface water residence time of the box (τ_{box} ; d). Equations 1 and 2 were simultaneously solved for each box
 220 under consideration to obtain surface water residence time and SGD flow. Note the first term on the right hand-side
 221 of each equation ($Q_{\text{WWTP}} * Ra_{\text{WWTP}}$) is only applicable to Cortiou (box 1; **Figure 1**). The mass balance for Cassis (box
 222 5) includes an additional advective input term from mixing with Port-Miou (box 4; **Figure 1**), where the $^{224,226}\text{Ra}$
 223 input to Cassis is equal to the $^{224,226}\text{Ra}$ export from Port-Miou (as calculated from Eqs. 1 & 2).

224 The mean ^{224}Ra and ^{226}Ra activities for each box (Ra_{box}) were calculated from a natural neighbor raster
 225 interpolation in ArcMap 10.1; minimum and maximum activities based on counting statistics were used to generate
 226 interpolation uncertainties. The volume of water impacted by SGD within each box (V) was assessed from vertical
 227 salinity profiles, determined at each station from the shipboard CTD sensor relative to Mediterranean seawater
 228 salinity. Stations T1-3, T2-4 and T9-2 (**Figure 1**) were averaged (\pm standard deviation) to determine the $^{224,226}\text{Ra}$
 229 endmember of open seawater in the region ($^{224}\text{Ra}_{\text{sea}} = 1.0 \pm 0.2$ dpm 100L⁻¹; $^{226}\text{Ra}_{\text{sea}} = 15 \pm 3$ dpm 100L⁻¹; salinity =
 230 37.9 ± 0.1 ; $n = 3$). Offshore seawater samples from T10 were appreciably enriched in groundwater-derived solutes
 231 and are therefore not included in the offshore seawater Ra average. Groundwater chemical element fluxes were
 232 determined for each box by multiplying the karstic spring solute concentration by the respective SGD flow for each
 233 box. The SGD flow and the chemical endmember uncertainty were propagated into the final solute flux uncertainty
 234 for each box. We assigned an apparent 50% uncertainty for surface water residence times, based on the analysis of
 235 Claude et al. (2019); box area and volumes are assigned an arbitrary uncertainty of 10%. Ra isotope endmembers for
 236 boxes 1 and 2 (where springs were not identified or sampled) are taken as the mean (\pm standard deviation) of the
 237 four springs sampled from boxes 4 and 5; Ra uncertainties for boxes 3 – 5 are based on analytical uncertainties
 238 (Garcia-Solsona et al., 2008). For solute endmembers (boxes 1, 2, 4 and 5), we simply use the mean (\pm standard
 239 deviation) of the four springs sampled from boxes 4 and 5 for each respective chemical element. Box 3 endmember
 240 concentrations are taken as the average of the two springs sampled from box 3 and uncertainties are approximately
 241 20% for macro-nutrients and 50% for micro-nutrients given their apparent range over distinct salinities (17.8 –
 242 26.3). Terms used in the mass balances and flux calculations are further described in **Section 3.4**.

243 3. Results

244 3.1 Hydrological and Meteorological Context

245 Figure 2 provides insight into the hydrological and meteorological contexts of the study. The Port-Miou
246 brackish spring's salinity remained almost constant and high (> 13) from October 2017 up to March 01 2018, which
247 represents a long-lasting drought period, which tends to cease in autumn for this Mediterranean climate. The Port-
248 Miou spring salinity is highly correlated with the discharge of the regional carbonate aquifer of Port-Miou (Arfib
249 and Charlier, 2016). Another proxy of the Port-Miou spring discharge is the Huveaune river discharge, which is
250 supplied by runoff during rainfall events and by continental karst springs within the watershed. The Huveaune river
251 exhibited a low discharge rate over the same period as the coastal karst spring of Port-Miou (inferred by elevated
252 salinities). During this high salinity period (6 months), 243 mm of precipitation occurred with a low daily intensity
253 (max 36 mm d^{-1} in Aubagne station). This precipitation recharged the soil and part of the unsaturated zone of the
254 carbonate aquifer, but it was not sufficient to activate the high seasonal flow stage (early spring; Figure 2).

255 From March 01 2018, rainfall events generated small floods in the Huveaune river and karst springs, with
256 minor contributions of the fast flow component (runoff in river or rapid karst groundwater flow, with a recession in
257 a few days) and a low increase of baseflow lasting for a few weeks. The rainfall event two weeks before the
258 sampling period (March 15th, 2018; 42 mm at Aubagne station and 64 mm at Plan d'Aups station; Figure 1)
259 generated a karst flood at the Port-Miou spring (Figure 2), as shown by the salinity decrease over four days,
260 followed by an increase in salinity until the next rainfall event (after the sampling period). The spring was then
261 recovering baseflow conditions by mixing of deep flows of brackish and fresh groundwater (Arfib and Charlier,
262 2016). Moreover, as inferred from the very low discharge of the Huveaune River ($< 1 \text{ m}^3 \text{ s}^{-1}$) during this time period
263 (Figure 2), the Cortiou sewage outfall to the sea was predominantly sourced from the WWTP and not from
264 additional mixing with the Huveaune and Jarret rivers.

265 The hydrological behavior of karst aquifers in the south of France has been previously studied and
266 successfully modeled, for instance in Fontaine de Vaucluse spring by Fleury et al., (2007b) (catchment area 1100
267 km²), Lez spring by Fleury et al. (2009) (catchment area 130 km²), Dardennes springs by Baudement et al. (2017)
268 (catchment area 70 km²), and Port-Miou by Arfib and Charlier (2016) (catchment area 400 km²). All of these
269 examples showed that more than 100 mm of cumulated rainfall is needed in autumn to begin recharging the karst
270 aquifer. Moreover, in a Mediterranean climate, daily rainfall events are commonly higher than tens of mm, and can
271 exceed 100 mm d^{-1} during extreme events. The period studied (2017 – 2018) was not subject to any extreme
272 precipitation event ($>100 \text{ mm d}^{-1}$; Figure 2). The rainfall event two weeks before the sampling period was thus a
273 standard precipitation event for the season and rapid karst groundwater discharging at the springs from the shallow
274 aquifer reservoir was thus minimal. With the preceding rainfall from September 2017 to March 2018, the aquifer
275 recovered from drought to low-flow, representative of baseflow conditions. Therefore, we argue that the measured
276 solute concentrations of the karstic springs are representative of baseflow conditions.

277 3.2 Biogeochemical Endmembers

278 Six different karstic springs of varying salinities (6.9 – 26.3) were sampled for chemical determinations
279 (dissolved and particulate nutrients, trace elements and Ra isotopes) during March 2018. In general, NO_3^- (24 – 81
280 μM), $\text{Si}(\text{OH})_4$ (60 – 110 μM) and PO_4^{3-} (0.15 – 0.46 μM) displayed the highest concentrations at the lowest salinities
281 and simply followed two-endmember linear mixing between brackish groundwaters and Mediterranean seawater
282 (Figure 3; Table 1). An opposite pattern was observed for NO_2^- ($\sim 0 - 0.06 \mu\text{M}$) and NH_4^+ (0.04 – 0.23 μM ; Table
283 1). Groundwater DIN:DIP ratios exhibited large variations (152 – 235; Table 1) but broadly fell along a dilution
284 trend [$(\text{N:P}) = -4.9582 * (\text{Salinity}) + 258.75$; $R^2 = 0.7521$; $p < 0.001$]. Karstic groundwater concentrations did not vary
285 greatly for DOC (40– 85 μM), POC (1.1 – 5.9 μM), DON (0.2 – 13.7 μM), PON (0.12 – 0.69 μM) and DOP (0.00 –
286 0.13 μM ; Table 2). Bacterial biomass ($0.99 * 10^5 \text{ cell mL}^{-1}$ for a salinity of 9.3) increased with increasing salinity to
287 $3.6 * 10^5 \text{ cell mL}^{-1}$ for a salinity of 35 (coastal seawater). Water samples collected at the outlet of the WWTP were
288 elevated in macro-nutrient concentrations (salinity = 21.7; Figure 3), reduced in DIN:DIP ratios (5; Table 1) and
289 significantly enriched in bacterial biomass (Table 2). Elevated salinities indicate rapid mixing of sewage effluent
290 with coastal seawater at the point of discharge.

291 Bioactive trace metals Mn, Fe, Co and Ni in karstic springs showed similar relationships as the dissolved
292 nutrients, with the greatest concentrations in water samples collected adjacent to the WWTP (Table 3; Figure 4).
293 Mn and Fe concentrations were lowest in Sugiton (7 and 17 nM; box 3) and similar between Port-Miou and Cassis
294 (Mn 13 – 17 nM; Fe 38 – 109 nM; boxes 4 & 5). Bioactive trace metals Cu and Zn displayed mid-salinity maxima
295 (Figure 4). There was a clear difference in groundwater Ra isotope activities between the three different Calanques,
296 while water samples collected near the WWTP outlet were relatively low in dissolved Ra (Figure 5). Brackish
297 groundwaters in Sugiton (box 3) were appreciably enriched in $^{224}\text{Ra}_{\text{ex}}$ (370 – 473 dpm 100L⁻¹) despite higher
298 salinities (Table 4).

3.3 Surface Waters

The salinity of coastal waters (< 4 km from shore) were lower than open Mediterranean seawaters (salinity = 38.2); the depth of waters influenced by SGD and/or sewage effluent varied from ~1 to ~5 m (**Figure 6**). Surface waters with reduced salinities were elevated in NO_3^- , PO_4^{3-} , and $\text{Si}(\text{OH})_4$ as a consequence of terrestrial (groundwater or WWTP) inputs, with lower concentrations at higher salinities (**Figure 3**). As a result, surface waters remain elevated in NO_3^- , PO_4^{3-} and $\text{Si}(\text{OH})_4$ (above open Mediterranean seawater concentrations) for up to several hundreds of meters beyond the point-source sewage outfall and karstic springs (boxes 4 and 5; **Figure 7**). Nutrient stoichiometric ratios indicate that surface waters and groundwaters were limited in DIP (mean DIN:DIP box 1 = 36; box 2 = 44; box 3 = 51; box 4 = 141; box 5 = 73) with the exception of three surface water samples collected in the vicinity of the sewage outfall, which were limited in DSi (**Figure 8**). Bioactive trace metals Mn, Fe, Co and Ni showed similar trends as major nutrients, with higher concentrations at lower salinities, albeit with greater variability (**Figure 4**). Cu and Zn showed the greatest variability in surface waters with several samples exceeding groundwater concentrations (**Figure 4**). Ra isotopes followed two-endmember linear mixing between brackish groundwaters and Mediterranean seawater (**Figure 5**). Surface water weighted average (\pm standard deviation) salinity, $^{224}\text{Ra}_{\text{ex}}$ and ^{226}Ra activities for each box are summarized in **Table 5**. Surface water parameters (salinity, pH, Ra isotopes, dissolved inorganic nutrients) are summarized in **Table S2**.

3.4 SGD flows and element fluxes

Surface water residence times varied widely, from 0.6 – 39 d, depending on the selected box (**Table 5**). Submarine groundwater discharge to the entire zone of the Calanques of Marseille-Cassis is estimated as $6.7 \pm 2.0 \text{ m}^3 \text{ s}^{-1}$ ($5.8 \pm 1.7 * 10^5 \text{ m}^3 \text{ d}^{-1}$) during the study period of March 2018, and is most prevalent along the eastern section of the studied area (**Table 5**). Claude et al. (2019) estimated a surficial spring discharge equal to $0.6 \pm 0.1 \text{ m}^3 \text{ s}^{-1}$ from a short-lived Ra mass balance to the Calanque of Port-Miou during baseflow conditions, compared to $1.0 \pm 0.3 \text{ m}^3 \text{ s}^{-1}$ during this study (box 4; **Table 5**). Just west of Marseille, Bejannin et al. (2020) estimated SGD equal to $\sim 0.6 \text{ m}^3 \text{ s}^{-1}$ along the karstic shoreline of Côte Bleue, or a factor of ten less than the Calanques of Marseille-Cassis. It is important to note that this SGD flow (and the chemical elements transported by SGD) is temporally variable; the shallow reservoir of the Port-Miou aquifer fluctuates in direct response to precipitation (**Figure 2**). The karstic groundwater DIN, DIP and DSi fluxes were $4.7 \pm 1.6 * 10^4 \text{ mol d}^{-1}$, $2.2 \pm 0.7 * 10^2 \text{ mol d}^{-1}$ and $6.3 \pm 2.0 * 10^4 \text{ mol d}^{-1}$, respectively, over the entire study area (**Figure 9**). Approximately 70% of the SGD inputs were into Cassis (box 5); area-normalized DIN and DIP fluxes to Cassis were thus $6,700 \pm 2,800 \text{ } \mu\text{mol N m}^{-2} \text{ d}^{-1}$ and $29 \pm 13 \text{ } \mu\text{mol P m}^{-2} \text{ d}^{-1}$, respectively (DIN:DIP >230).

4. Discussion

4.1 Biogeochemical signature of the karst springs and coastal waters

The karstic springs were dominated by NO_3^- , with negligible NO_2^- and NH_4^+ , indicative of a highly oxygenated aquifer system where there is little denitrification, typical of Mediterranean karst aquifers. The relatively low NO_3^- concentrations of the springs, coupled with a lack of surface water inputs, suggest that the NO_3^- is naturally derived (*i.e.* atmosphere-aquifer interactions; Garcia-Solsona et al., 2010a,b), rather than of an anthropogenic origin. In comparison, concentrations of DSi for all springs were relatively high, reflecting near-saturated equilibrium conditions with the karst aquifer matrix (*i.e.* water-rock interactions) as noted by Tamborski et al. (2018). Low groundwater DIP concentrations for all of the springs are typical of karst aquifers where DIP may co-precipitate with dissolved Ca (Slomp and van Cappellen, 2004).

The karstic spring nutrient concentrations of the Calanques of Marseille-Cassis (**Table 1**) are comparable to other karstic springs in the southern Gulf of Lions region, and more broadly to that of the entire Mediterranean Sea (excluding DIN). For example, karst springs and shallow pore water nutrient concentrations were recently investigated along Côte Bleue, a 22 km long stretch of karstic coastline just west of Marseille (Bejannin et al., 2020). Brackish springs were appreciably enriched in $\text{Si}(\text{OH})_4$ ($113 \pm 40 \text{ } \mu\text{M}$) but not NO_3^- ($0.02 - 4.26 \text{ } \mu\text{M}$), whereas brackish pore waters exhibited a wide range in all macro-nutrients ($2 - 133 \text{ } \mu\text{M Si}(\text{OH})_4$; $22 - 194 \text{ } \mu\text{M NO}_3^- + \text{NO}_2^-$; $0.01 - 4.0 \text{ } \mu\text{M PO}_4^{3-}$). Macro-nutrient concentrations of the studied springs here are comparable to the karst brackish groundwater spring (salinity $\sim 4 - 10$) of La Palme lagoon ($\sim 200 \text{ km west, western Gulf of Lions}$), with $\text{Si}(\text{OH})_4$, NO_3^- and PO_4^{3-} concentrations of $114 \text{ } \mu\text{M}$, $50 - 62 \text{ } \mu\text{M}$ and $0.10 - 0.43 \text{ } \mu\text{M}$, respectively (Rodellas et al., 2018; Tamborski et al., 2018). Chen et al. (2020) recently compiled karstic spring nutrient concentrations for 31 different locations along the Mediterranean Sea. Regional DIN concentrations ($120 - 440 \text{ } \mu\text{M}$; salinity < 10; 1st and 3rd quartiles) are appreciably higher than the karst springs studied here over a similar salinity range, while DIP ($0.18 - 0.72 \text{ } \mu\text{M}$) concentrations are comparable (**Table 1**).

There was an increase in NO_2^- and NH_4^+ concentrations along the salinity gradient (excluding sewage-impacted samples), where the karstic springs exhibited lower concentrations than Mediterranean seawater (**Figure 3**). This observation is coherent with an autochthonous production of NO_2^- and NH_4^+ during mixing, rather than a

355 terrestrial NO_2^- and NH_4^+ source. Indeed, bacterial biomass increased linearly along the salinity gradient (**Figure 3**).
356 The bacterial compartment must behave as a nitrogen producer and not as a consumer. Pujo-Pay et al. (2006)
357 showed that there is a threshold value for the DOC:DON ratio as an indicator of the trophic role of bacteria. A
358 DOC:DON ratio below 10 indicates that bacteria meet their nitrogen needs for growth and are therefore a source of
359 nitrogen to the ecosystem (ammonification process). Above 10, bacteria need to consume nitrogen to balance their
360 internal needs and therefore consume DIN. The DOC:DON ratio is 0.6 for sewage effluent, 3 to 6 for Port-Miou
361 (box 4), ~14 for Sugiton (box 3), and higher than 15 for surface and coastal waters (**Table 2**).

362 Karstic spring Fe concentrations (17 – 109 nM) were lower than karstic springs previously investigated in
363 the Northwest Mediterranean (130 – 550 nM; $n = 12$; 1st – 3rd quartiles; Trezzi et al., 2016), although the springs
364 investigated here are more saline (6.9 – 26.3 vs. 4.1 – 5.3; 1st – 3rd quartiles; Trezzi et al., 2016). Karstic
365 groundwater Co and Ni concentrations were within the range of concentrations reported for the Northwest
366 Mediterranean springs (Co = 0.14 – 0.54 nM; Ni = 2.7 – 7.9 nM), despite their higher salinity. Karstic springs for
367 this study were higher in Cu (2 – 18 nM) and Zn (5 – 109 nM) compared to the range reported by Trezzi et al.
368 (2016) (Cu = 2.1 – 4.6 nM; Zn = 33 – 71 nM). The karstic spring trace metal concentration ranges suggest that these
369 bioactive metals are derived from either atmosphere-aquifer interactions or water-rock interactions, and do not
370 reflect an anthropogenic contaminant source (Alorda-Kleinglass et al., 2019; Trezzi et al., 2016). Surface water mid-
371 salinity maxima of Zn and Cu in Port-Miou and Cassis (boxes 4 and 5) are positive linearly correlated (excluding
372 one outlier; $R^2 = 0.95$; $P < 0.01$). Zn and Cu may be derived from antifouling paints (Charette and Buesseler, 2004;
373 Garcia-Orellana et al., 2011) from a high density of residential boats moored in both the Calanque of Port-Miou and
374 in Cassis harbor.

375 Karstic groundwater Ra isotope activities (**Table 4, Figure 5**) are in general agreement with previous
376 studies for the Calanque of Port-Miou (Bejannin et al., 2017; Claude et al., 2019). The relatively lower ^{226}Ra
377 activities of the Bestouan submarine spring (box 5; 318 – 324 dpm 100L^{-1}), as compared to the Port-Miou spring
378 (box 4; 506 – 525 dpm 100L^{-1} , box 4; **Table 4**) is a function of the salinity of the groundwater and its origin (Romey
379 et al., 2014). Although both the Bestouan and Port-Miou springs share a common recharge area, the brackish
380 groundwater of the Bestouan spring originates from a freshwater surface stream 2 km inland from the sea that
381 infiltrates into the karst, where it mixes with a deeper reservoir and thus decreases the salinity of the deep brackish
382 groundwater. Therefore, the ^{226}Ra activity of the Port-Miou spring is likely higher because it is only a mixture
383 between deep circulated seawater and fresh groundwater, whereas the Bestouan spring is mixed with a third surficial
384 component with relatively low ^{226}Ra activity.

385 4.2 Chemical fluxes from SGD, WWTP and atmospheric deposition

386 To determine the relative significance of macro and micro-nutrient fluxes associated with submarine karstic
387 springs to the Calanques of Marseille-Cassis, we compared the magnitude of groundwater nutrient loads to that of
388 the WWTP of Cortiou and from atmospheric deposition. Previous studies estimated dissolved and particulate solute
389 fluxes from the Cortiou sewage outfall during the dry season (~250,000 $\text{m}^3 \text{d}^{-1}$; Oursel et al., 2014, 2013). Dust
390 deposition, particularly from the Sahara Desert, may represent a potentially significant source of chemical elements
391 to the Mediterranean Sea and fluxes are likely more significant under intense rainfall (Durrieu de Madron et al.,
392 2011; Garcia-Orellana et al., 2006). Nutrient and trace metal total (wet and dry) atmospheric depositional fluxes
393 were compiled from the literature for nearby regions (**Table S3**). Atmospheric deposition fluxes were calculated
394 considering a coastal surface area of 23.1 km^2 (boxes 1 – 5; **Figure 1**). It is important to note that we assume that the
395 atmospheric deposition fluxes are representative of the total (wet and dry) depositional processes occurring in the
396 coastal zone of the Calanques of Marseille-Cassis during the study period; atmospheric and WWTP fluxes serve
397 only as first-order approximations.

398 Macro- and micro-nutrient fluxes from SGD, WWTP and atmospheric deposition to the Calanques of
399 Marseille-Cassis are summarized in **Figure 9**. The karstic groundwater solute fluxes calculated in this study are a
400 snapshot view that we consider near representative of baseflow conditions for the Calanques of Marseille-Cassis
401 (**Figure 2**). In general, WWTP macro- and micro-nutrient loads exceeded inputs from karstic groundwaters during
402 the studied period, except for DSi. In contrast, groundwater solute fluxes generally exceeded inputs from total
403 atmospheric deposition, aside from dissolved Fe (**Figure 9 a,b**). Macro-nutrient groundwater loads to Cassis (box 5)
404 are normalized to the shoreline length of the considered box (6 km), resulting in $\text{Si}(\text{OH})_4$ and NO_3^- fluxes of 11 ± 3
405 $\cdot 10^3 \text{ mol d}^{-1} \text{ km}^{-1}$ and $8 \pm 3 \cdot 10^3 \text{ mol d}^{-1} \text{ km}^{-1}$, respectively. These karst groundwater baseflow nutrient fluxes are
406 comparable to karst groundwater $\text{Si}(\text{OH})_4$ ($6.2 \pm 5.0 \cdot 10^3 \text{ mol d}^{-1} \text{ km}^{-1}$) and $\text{NO}_3^- + \text{NO}_2^-$ ($4.0 \pm 2.0 \cdot 10^3 \text{ mol d}^{-1} \text{ km}^{-1}$)
407 loads to Côte Bleue (just west of Marseille), assessed over multiple seasons (Bejannin et al., 2020), and are similar
408 to flux estimates from a sandy alluvial shoreline farther west along the Gulf of Lions ($2.4 \pm 1.4 \cdot 10^3 \text{ mol Si d}^{-1} \text{ km}^{-1}$
409 and $5.7 \pm 3.2 \cdot 10^3 \text{ mol N d}^{-1} \text{ km}^{-1}$; Tamborski et al., 2018). Interestingly, Bejannin et al. (2020) note that these point-

410 source karstic spring macro-nutrient fluxes are comparable to fluxes along the sandy alluvial shoreline of La Palme
411 to the west, within the Gulf of Lions, where nutrient loads are thought to be driven by a combination of subsurface
412 lagoon-seawater exchange and seawater circulation through permeable coastal sediments (Tamborski et al., 2019,
413 2018).

414 Sewage inputs occur along the western region of the Calanques (box 1; **Figure 1**) while karstic
415 groundwaters more broadly impact the entire coastal zone (**Figure 7**), and are greatest along the eastern region,
416 particularly from the springs of Port-Miou and Cassis (boxes 4 & 5; **Table 5**). The significance of atmospheric
417 deposition, as compared to SGD and riverine inputs, is proportional to the area under consideration; the larger
418 offshore area considered, the more significant atmospheric trace metal deposition becomes (Trezzi et al., 2016). For
419 the entire Mediterranean Sea, DIN and DSi inputs from SGD are estimated to be significantly greater than
420 atmospheric deposition, while DIP inputs are similar (Rodellas et al., 2015). For the Calanques of Marseille-Cassis,
421 atmospheric deposition is negligible over a spatial scale of meters to hundreds of meters away from the karstic
422 springs, where groundwater (or sewage) is the dominant vector of solute transport to the coastal ocean (e.g. **Figure**
423 **7**). The area-normalized DIN ($6,700 \pm 2,800 \mu\text{mol N m}^{-2} \text{d}^{-1}$) and DIP ($29 \pm 13 \mu\text{mol P m}^{-2} \text{d}^{-1}$) fluxes to Cassis (box
424 5) are one order of magnitude greater than atmospheric deposition (**Table S3**).

425 4.3 Significance of Chemical Fluxes

426 4.3.1 Major Nutrient Fluxes

427 The Mediterranean Sea is primarily limited in phosphorous (Krom et al., 1991; Pujo-Pay et al., 2011);
428 therefore, any DIP input from karstic springs or sewage to the coastal sea should be considered potentially
429 significant, as it may change the geochemical conditions of the water column (**Figure 8**). DIP mixing plots for Port-
430 Miou and Cassis indicate significant DIP concentrations in brackish surface waters during the studied period
431 (**Figure 3**); therefore, the impact of SGD in supplying DIP (and other solutes) occurs over a scale of several
432 kilometers (from at least 6 individual springs), despite being point-sources (**Figure 7**). As a first-order
433 approximation, we can evaluate how much DIP is removed by primary production from a coastal DIP budget (Kim
434 et al., 2011; Luo et al., 2014) considering equation (3),

$$435 P_{SGD} + P_{WWTP} + P_{atm} - P_{mix} = P_{uptake} \quad (\text{Eq. 3})$$

436 where P_{SGD} , P_{WWTP} , P_{atm} , P_{mix} and P_{uptake} are the DIP fluxes (mol d^{-1}) to each respective box from SGD, the WWTP,
437 total atmospheric deposition, mixing losses with offshore seawater and uptake from biological production,
438 respectively. DIP inputs from SGD, the WWTP and total atmospheric deposition have been previously evaluated
439 (Sections 3.4 & 4.2; **Figure 9**). The loss of DIP from mixing with offshore Mediterranean seawater is evaluated
440 similarly to the mixing loss of Ra (Eqs. 1 & 2), taken as the concentration difference between the mean DIP
441 concentration in each coastal box and offshore Mediterranean seawater ($0.025 \mu\text{M}$), with respect to the volume of
442 water impacted by groundwater and the surface water residence time (**Table 5**).

443 During baseflow conditions, SGD is relatively insignificant in the DIP budget of the western Calanques and
444 becomes increasingly more important in the eastern Calanques; the relative percent contribution of each DIP source
445 and sink is shown in **Figure 10**. In Sugiton (box 3), DIP is rapidly removed within the first 10 m of the karstic
446 springs (**Figure 7**), with groundwater sustaining 7 (± 1) % of the DIP uptake. Mixing losses approximately balance
447 groundwater DIP inputs to Port-Miou (i.e. no biological consumption; box 4), unsurprising given the relatively short
448 surface water residence time ($0.6 \pm 0.3 \text{ d}$; **Table 5**) and the observed conservative behavior of DIP, with respect to
449 groundwater-seawater mixing (**Figure 3**, **Figure 7**). Importantly, this suggests that groundwater-derived DIP may
450 persist in the coastal ocean for at least a half day before it is significantly impacted by primary producers. In
451 comparison, SGD accounts for more than 100% of the DIP uptake in Cassis (box 5) where surface water residence
452 times exceed 2 days (**Table 5**), with a net consumption of $140 \pm 220 \text{ mol P d}^{-1}$ (**Figure 10**). The large uncertainty is
453 derived from the additional mixing term between Port-Miou and Cassis (boxes 4 and 5), and between Cassis and the
454 open Mediterranean Sea.

455 The groundwater DIP flux to the 20 km shoreline of the Calanques of Marseille-Cassis accounts for only
456 2.7 (± 1.0) % of the total DIP uptake ($8.3 \pm 6.9 * 10^3 \text{ mol d}^{-1}$) during baseflow conditions, unsurprising as the sewage
457 DIP flux is two orders of magnitude greater than SGD (**Figure 9**). Assuming a Redfield Ratio of 106:16:1.0 (C:N:P)
458 for phytoplankton (Pujo-Pay et al., 2011) and assuming that all of the DIP supplied is utilized by biological
459 production, then primary production supported by sewage DIP loading equals $1,900 \pm 1,600 \text{ mg C m}^{-2} \text{d}^{-1}$ over the
460 surface area of Cortiou (box 1). However, three surface water samples collected near the sewage outfall were limited
461 in DSi (**Figure 8**), suggesting the above primary production estimate may be too high. DSi limitation in Cortiou is
462 ultimately driven by the extreme DIN and DIP sewage loads (**Figures 3 & 9**).

463 Considering the surface area of Cassis (box 5), the primary production associated with DIP consumption is
464 $33 \pm 52 \text{ mg C m}^{-2} \text{ d}^{-1}$, or ~1% of the total production stimulated by sewage effluent DIP loading to Cortiou (box 1).
465 This rate of primary production is similar to other coastal environments impacted by SGD, as summarized by Wang
466 et al. (2018). Thus, while the groundwater DIP flux to the Calanque of Cassis is small compared to the WWTP, it is
467 nonetheless significant at a local and regional-scale in supporting primary production during baseflow conditions
468 (**Figures 9 & 10**). Similarly, the groundwater DIN ($3.6 \pm 1.5 * 10^4 \text{ mol d}^{-1}$) and DSi ($4.7 \pm 2.0 * 10^4 \text{ mol d}^{-1}$) loads to
469 Cassis (box 5) may help sustain biological production, as there are no other major nutrient sources in this region.
470 SGD may further facilitate primary production in the days immediately following a rainfall event (**Figure 2**),
471 assuming that the karstic spring nutrient concentrations are not significantly diluted. Note that certain algal species
472 may be physically impacted by the presence of karstic springs, irrespective of nutrient loading, through
473 environmental gradients in pH, oxygen or salinity (Foley, 2018; Lecher et al., 2018). For example, Cochu et al.
474 (2013) concluded that reduced salinity from the Bestouan karstic spring retarded the development of the harmful
475 algae *Ostreopsis cf. ovata* in Cassis because the dinoflagellate is more adapted to marine environmental conditions,
476 despite excess NO_3^- and Si(OH)_4 inputs from groundwaters. Thus, SGD may also negatively impact certain
477 phytoplankton and bacteria species development by altering local environmental gradients (e.g. **Figure 3**); this topic
478 requires further study.

479 4.3.2 Micro Nutrient Fluxes

480 Groundwater Mn and Fe fluxes are one order of magnitude lower than sewage fluxes during baseflow
481 conditions (**Figure 9**). Groundwater Fe may be derived from aquifer mineral weathering or atmosphere-aquifer
482 interactions. Fe is typically added as a flocculant during wastewater treatment, which likely explains the high
483 concentrations observed near the sewage outlet (**Figure 4**). Similar to DIP, the SGD-driven Fe flux ($48 \pm 21 \text{ mol d}^{-1}$)
484 primarily occurs along the eastern region of the Calanques, whereas sewage inputs dominate farther west (640 ± 180
485 mol d^{-1}) with considerable inputs from atmospheric deposition ($230 \pm 160 \text{ mol d}^{-1}$) over the entire coastal area
486 (**Figure 9**). It remains to be seen what proportion of Fe supplied by atmospheric deposition is bioavailable.
487 Atmospheric Fe loads to the Mediterranean Sea are seasonally variable, and surface water Fe concentrations are
488 typically lowest during spring blooms (Bonnet and Guieu, 2006). Increased Fe loading from SGD during the spring
489 may play an important role in regulating primary production, particularly after a heavy rainfall event (i.e. **Figure 2**).
490 The karstic springs investigated here have Fe:P ratios between 0.11 and 0.24, and Fe:N ratios between 710 and
491 2140. Such ratios demonstrate an abundance of Fe; indeed, coastal seawater Fe:P (0.12 – 0.80) and Fe:N (2 – 800)
492 ratios suggests that Fe was not limiting primary production during the studied baseflow period. However, relatively
493 high Fe may locally enhance nitrogen fixation (Bonnet and Guieu, 2006). The SGD area-normalized Fe flux is 7 ± 4
494 $\mu\text{mol m}^{-2} \text{ d}^{-1}$ to Cassis (box 5), within the range reported by Trezzi et al. (2016) to the NW Mediterranean Sea.

495 Sewage inputs of Co, Ni and Cu were approximately one order of magnitude greater than SGD, while Zn
496 inputs were similar (**Figure 9**). Oursel et al. (2014) analyzed particles adjacent to the Cortiou sewage outlet (box 1)
497 and found that Cu, Ni and Zn were anthropogenically derived from non-treated sewage. Sewage effluent has
498 fundamentally altered the structure of local benthic communities in the vicinity of the Cortiou sewage outfall (Bellan
499 et al., 1999). It is unlikely that SGD plays a major role in supplying these trace elements to the western Calanques;
500 however, trace metal fluxes may be significant in the eastern Calanques adjacent to the Port-Miou and Bestouan
501 springs (**Figures 4 & 9**).

502 Antifouling boat paint is a potential source of Cu and Zn (Charette and Buesseler, 2004; Garcia-Orellana et al.,
503 2011), as the Calanque of Port-Miou and Cassis both host several dozen boats. We can simply compare the Cu and
504 Zn inventory supplied by SGD (SGD element flux * surface water residence time) to the total element inventory
505 observed in the Calanque of Port-Miou (box 4). The total inventory is calculated as the excess metal concentration
506 (mean concentration minus Mediterranean seawater; n = 6) multiplied by the volume of water impacted by
507 groundwater; note that this simple calculation does not account for the complex biogeochemical cycling of these
508 metals (Rodellas et al., 2014). For the Calanque of Port-Miou, SGD supplies 1 (± 1) % of the Cu inventory and 11
509 (± 12) % of the Zn inventory. Thus, SGD is relatively minor in the transfer of these bioactive metals to the coastal
510 Mediterranean Sea here.

511 5. Summary & Conclusions

512 Coastal-zone primary production can be sustained by the allochthonous nutrient and bioactive trace metal fluxes
513 from karstic springs, particularly in oligotrophic environments like the Mediterranean Sea. For the Calanques of
514 Marseille-Cassis, groundwater discharge is highly variable in time, as inferred from *in-situ* salinity measurements of
515 the first-order Port-Miou spring. It remains to be seen how element fluxes may impact primary production at
516 different times of the year, for example after a strong precipitation event or during the summer when the water
517 column is stratified due to the permanent presence of a thermocline. Under wet season baseflow conditions (March
518 2018), major nutrient and bioactive trace metal inputs were dominated by sewage effluent, aside from DSi, with

519 minor contributions from atmospheric deposition. However, outside of the influence of sewage effluent,
520 groundwater became the dominant nutrient vector and supported between 7 and ~100% of the estimated primary
521 production, depending upon the Calanque. At a local-scale, karstic groundwater springs reduce P-limitation and
522 supply excess Fe, which may locally enhance nitrogen fixation. The karstic springs studied here also broadly serve
523 to provide new chemical elements to the Mediterranean Sea, thereby impacting the various element (and potentially
524 isotopic) budgets.

525 6. Acknowledgements

526 This study was funded by the MED-SGD project funded by ANR (ANR-15-CE01-0004; PI: Pieter van Beek). The
527 postdoctoral fellowship of Joseph Tamborski is supported by FEDER funded by Europe and Région Occitanie
528 Pyrénées-Méditerranée (SELECT project; PIs: Pieter van Beek and Marc Souhaut). Jordi Garcia Orellana wants to
529 thank the support of the Generalitat de Catalunya to MERS (2018 SGR-1588). This work is contributing to the
530 ICTA ‘Unit of Excellence’ (MinECo, MDM2015-0552). This work benefited from the Port-Miou in-situ
531 observatory within the framework of the KARST observatory network (www.sokarst.org) initiative from the
532 INSU/CNRS. Rainfall data are provided by Météo-France. We thank the captain and crew of RV Antédon II for
533 help during sampling at sea, including Simon Bejannin and Emilie Le Roy at LEGOS. We thank Dorian Guillemain,
534 Nagib Bhairy, Deny Malengros and Christian Grenz at MIO for providing the CTD data. We thank Remi Freydier at
535 AETE-ISO Platform, OSU-OREME/Université de Montpellier, for performing trace element analyses and Olivier
536 Crispi at LOMIC, Banyuls-sur-Mer.

537 7. References

- 538 Alorda-Kleinglass, A., Garcia-Orellana, J., Rodellas, V., Cerdà-Domènech, M., Tovar-Sánchez, A., Diego-Feliu, M.,
539 Trezzi, G., Sánchez-Quilez, D., Sanchez-Vidal, A., Canals, M., 2019. Remobilization of dissolved metals from
540 a coastal mine tailing deposit driven by groundwater discharge and porewater exchange. *Science of the Total*
541 *Environment* 688, 1359–1372. <https://doi.org/10.1016/j.scitotenv.2019.06.224>
- 542 Aminot, A., Kerouel, R., 2007. Dosage automatique des nutriments dans les eaux marines: méthodes en flux
543 continu. Ed. Ifremer, Méthodes d’analyse en milieu marin, 188 pp.
- 544 Arfib, B., Charlier, J.-B., 2016. Insights into saline intrusion and freshwater resources in coastal karstic aquifers
545 using a lumped Rainfall-Discharge-Salinity model (the Port-Miou brackish spring, SE France). *Journal of*
546 *Hydrology* 540, 148–161. <https://doi.org/10.1016/j.jhydrol.2016.06.010>
- 547 Bakalowicz, M., 2015. Karst and karst groundwater resources in the Mediterranean. *Environmental Earth Sciences*
548 74, 5–14. <https://doi.org/10.1007/s12665-015-4239-4>
- 549 Baudement, C., Arfib, B., Mazzilli, N., Jouves, J., Lamarque, T., Guglielmi, Y., 2017. Groundwater management of
550 a highly dynamic karst by assessing baseflow and quickflow with a rainfall-discharge model (Dardennes
551 springs, SE France) 188, 40. <https://doi.org/10.1051/bsgf/2017203>
- 552 Bejannin, S., Tamborski, J.J., van Beek, P., Souhaut, M., Stieglitz, T., Radakovitch, O., Claude, C., Conan, P., Pujot-
553 Pay, M., Crispi, O., le Roy, E., Estournel, C., 2020. Nutrient Fluxes Associated With Submarine Groundwater
554 Discharge From Karstic Coastal Aquifers (Côte Bleue, French Mediterranean Coastline). *Frontiers in*
555 *Environmental Science* 7. <https://doi.org/10.3389/fenvs.2019.00205>
- 556 Bejannin, S., van Beek, P., Stieglitz, T., Souhaut, M., Tamborski, J., 2017. Combining airborne thermal infrared
557 images and radium isotopes to study submarine groundwater discharge along the French Mediterranean
558 coastline. *Journal of Hydrology: Regional Studies* 13. <https://doi.org/10.1016/j.ejrh.2017.08.001>
- 559 Bellan, G., Bourcier, M., Salen-Picard, C., Arnoux, A., Casserley, S., 1999. Benthic ecosystem changes associated
560 with wastewater treatment at Marseille: Implications for the protection and restoration of the Mediterranean
561 coastal shelf ecosystems. *Water Environment Federation* 71, 483–493.
- 562 Blavoux, B., Gilli, E., Rousset, C., 2004. Alimentation et origine de la salinité de la source sous-marine de Port-
563 Miou (Marseille–Cassis). Principale émergence d’un réseau karstique hérité du Messinien. *C.R. Geoscience*
564 336, 523–533. <https://doi.org/10.1016/j.crte.2003.10.027>
- 565 Bonnet, S., Guieu, C., 2006. Atmospheric forcing on the annual iron cycle in the western Mediterranean Sea: A 1-
566 year survey. *Journal of Geophysical Research* 111, C09010. <https://doi.org/10.1029/2005JC003213>
- 567 Cavalera, T., 2007. Etude du fonctionnement et du bassin d’alimentation de la source sous-marine de Port Miou
568 (Cassis, Bouches-du-Rhône). Approche multicritère. Université de Provence - Aix-Marseille.

- 569 Charette, M. a, Moore, W.S., Burnett, W.C., 2007. CHAPTER-5 Uranium-and Thorium- Series Nuclides as Tracers
570 of Submarine Groundwater Discharge CHAPTER-5 Uranium-and Thorium-Series Nuclides as Tracers of
571 Submarine Groundwater Discharge. *Radioactivity in the Environment* 13, 234–289.
572 [https://doi.org/10.1016/S1569-4860\(07\)00005-8](https://doi.org/10.1016/S1569-4860(07)00005-8)
- 573 Charette, M.A., Buesseler, K.O., 2004. Submarine groundwater discharge of nutrients and copper to an urban
574 subestuary of Chesapeake Bay (Elizabeth River). *Limnology and Oceanography* 49, 376–385.
575 <https://doi.org/10.4319/lo.2004.49.2.0376>
- 576 Chen, X., Cukrov, Neven, Santos, I.R., Rodellas, V., Cukrov, Nuša, Du, J., 2020. Karstic submarine groundwater
577 discharge into the Mediterranean: Radon-based nutrient fluxes in an anchialine cave and a basin-wide
578 upscaling. *Geochimica et Cosmochimica Acta* 268, 467–484. <https://doi.org/10.1016/J.GCA.2019.08.019>
- 579 Claude, C., Cockenpot, S., Arfib, B., Meulé, S., Radakovitch, O., 2019. Accuracy and sensitivity of radium mass
580 balances in assessing karstic submarine groundwater discharge in the stratified Calanque of Port-Miou
581 (Mediterranean Sea). *Journal of Hydrology* 578, 124034. <https://doi.org/10.1016/J.JHYDROL.2019.124034>
- 582 Coahu, S., Mangialajo, L., Thibaut, T., Blanfuné, A., Marro, S., Lemé, R., 2013. Proliferation of the toxic
583 dinoflagellate *Ostreopsis cf. ovata* in relation to depth, biotic substrate and environmental factors in the North
584 West Mediterranean Sea. <https://doi.org/10.1016/j.hal.2013.01.002>
- 585 Conan, P., Søndergaard, M., Kragh, T., Thingstad, F., Pujo-Pay, M., Williams, P.J. le B., Markager, S., Cauwet, G.,
586 Borch, N.H., Evans, D., Riemann, B., 2007. Partitioning of organic production in marine plankton
587 communities: The effects of inorganic nutrient ratios and community composition on new dissolved organic
588 matter. *Limnology and Oceanography* 52, 753–765. <https://doi.org/10.4319/lo.2007.52.2.0753>
- 589 Custodio, E., 2010. Coastal aquifers of Europe: an overview. *Hydrogeology Journal* 18, 269–280.
590 <https://doi.org/10.1007/s10040-009-0496-1>
- 591 de Jonge, V.N., Villerius, L.A., 1989. Possible role of carbonate dissolution in estuarine phosphate dynamics.
592 *Limnology and Oceanography* 34, 332–340. <https://doi.org/10.4319/lo.1989.34.2.0332>
- 593 Diaz, F., Raimbault, P., Conan, P., 2000. Small-scale study of primary productivity during spring in a Mediterranean
594 coastal area (Gulf of Lions). *Continental Shelf Research* 20, 975–996. [https://doi.org/10.1016/S0278-4343\(00\)00006-6](https://doi.org/10.1016/S0278-4343(00)00006-6)
- 596 Diego-Feliu, M., Rodellas, V., Alorda-Kleinglass, A., Tamborski, J., van Beek, P., Heins, L., Bruach J.M., Arnold,
597 R., Garcia-Orellana, J., 2020. Guidelines and limits for the quantification of U/Th series radionuclides with the
598 radium delayed coincidence counter (RaDeCC). *Journal of Geophysical Research: Oceans* 125.
599 <https://doi.org/https://doi.org/10.1029/2019JC015544>
- 600 Durrieu de Madron, X., Guieu, C., Sempéré, R., Conan, P., Cossa, D., D’Ortenzio, F., Estournel, C., Gazeau, F.,
601 Rabouille, C., Stemann, L., Bonnet, S., Diaz, F., Koubbi, P., Radakovitch, O., Babin, M., Baklouti, M.,
602 Bancon-Montigny, C., Belviso, S., Bensoussan, N., Bonsang, B., Bouloubassi, I., Brunet, C., Cadiou, J.F.,
603 Carlotti, F., Chami, M., Charmasson, S., Charrière, B., Dachs, J., Doxaran, D., Dutay, J.C., Elbaz-Poulichet,
604 F., Eléaume, M., Eyrolles, F., Fernandez, C., Fowler, S., Francour, P., Gaertner, J.C., Galzin, R., Gasparini, S.,
605 Ghiglione, J.F., Gonzalez, J.L., Goyet, C., Guidi, L., Guizien, K., Heimbürger, L.E., Jacquet, S.H.M., Jeffrey,
606 W.H., Joux, F., le Hir, P., Leblanc, K., Lefèvre, D., Lejeune, C., Lemé, R., Loÿe-Pilot, M.D., Mallet, M.,
607 Méjanelle, L., Mélin, F., Mellon, C., Mérigot, B., Merle, P.L., Migon, C., Miller, W.L., Mortier, L., Mostajir,
608 B., Mousseau, L., Moutin, T., Para, J., Pérez, T., Petrenko, A., Poggiale, J.C., Prieur, L., Pujo-Pay, M., Pulido-
609 Villena, Raimbault, P., Rees, A.P., Ridame, C., Rontani, J.F., Ruiz Pino, D., Sicre, M.A., Taillandier, V.,
610 Tamburini, C., Tanaka, T., Taupier-Letage, I., Tedetti, M., Testor, P., Thébaud, H., Thouvenin, B., Touratier,
611 F., Tronczynski, J., Ulses, C., van Wambeke, F., Vantrepotte, V., Vaz, S., Verney, R., 2011. Marine
612 ecosystems’ responses to climatic and anthropogenic forcings in the Mediterranean. *Progress in*
613 *Oceanography*. <https://doi.org/10.1016/j.pocean.2011.02.003>
- 614 Egger, M., Jilbert, T., Behrends, T., Rivard, C., Slomp, C.P., 2015. Vivianite is a major sink for phosphorous in
615 methanogenic coastal surface sediments. *Geochimica et Cosmochimica Acta*.
616 <https://doi.org/http://dx.doi.org/10.1016/j.gca.2015.09.012>
- 617 Fleury, P., Bakalowicz, M., de Marsily, G., 2007a. Submarine springs and coastal karst aquifers: A review. *Journal*
618 *of Hydrology* 339, 79–92. <https://doi.org/10.1016/J.JHYDROL.2007.03.009>

- 619 Fleury, P., Ladouche, B., Conroux, Y., Jourde, H., Dörfli, N., 2009. Modelling the hydrologic functions of a karst
620 aquifer under active water management – The Lez spring. *Journal of Hydrology* 365, 235–243.
621 <https://doi.org/10.1016/J.JHYDROL.2008.11.037>
- 622 Fleury, P., Plagnes, V., Bakalowicz, M., 2007b. Modelling of the functioning of karst aquifers with a reservoir
623 model: Application to Fontaine de Vaucluse (South of France). *Journal of Hydrology* 345, 38–49.
624 <https://doi.org/10.1016/J.JHYDROL.2007.07.014>
- 625 Foley, L., 2018. Karst-channelled intertidal submarine groundwater discharge (SGD) conditions the form of the rock
626 pool sessile assemblage. *Estuarine, Coastal and Shelf Science*. <https://doi.org/10.1016/J.ECSS.2018.08.014>
- 627 Garcia-Orellana, J., Cañas, L., Masqué, P., Obrador, B., Olid, C., Pretus, J., 2011. Chronological reconstruction of
628 metal contamination in the Port of Maó (Minorca, Spain). *Marine Pollution Bulletin* 62, 1632–1640.
629 <https://doi.org/10.1016/J.MARPOLBUL.2011.06.013>
- 630 Garcia-Orellana, J., Sanchez-Cabeza, J.A., Masqué, P., Àvila, A., Costa, E., Loÿe-Pilot, M.D., Bruach-Menchén,
631 J.M., 2006. Atmospheric fluxes of ²¹⁰Pb to the western Mediterranean Sea and the Saharan dust influence.
632 *Journal of Geophysical Research* 111, D15305. <https://doi.org/10.1029/2005JD006660>
- 633 Garcia-Solsona, E., Garcia-Orellana, J., Masque, P., Dulaiova, H., 2008. Uncertainties associated with Ra-223 and
634 Ra-224 measurements in water via a Delayed Coincidence Counter (RaDeCC). *Marine Chemistry* 109, 198–
635 219. <https://doi.org/10.1016/j.marchem.2007.11.006>
- 636 Garcia-Solsona, E., Garcia-Orellana, J., Masque, P., Garces, E., Radakovitch, O., Mayer, A., Estrade, S.,
637 Basterretxea, G., 2010a. An assessment of karstic submarine groundwater and associated nutrient discharge to
638 a Mediterranean coastal area (Balearic Islands, Spain) using radium isotopes. *Biogeochemistry* 97, 211–229.
639 <https://doi.org/10.1007/s10533-009-9368-y>
- 640 Garcia-Solsona, E., Garcia-Orellana, J., Masque, P., Rodellas, V., Mejias, M., Ballesteros, B., Dominguez, J.A.,
641 2010b. Groundwater and nutrient discharge through karstic coastal springs (Castello, Spain). *Biogeosciences*
642 7, 2625–2638. <https://doi.org/10.5194/bg-7-2625-2010>
- 643 Geibert, W., Rodellas, V., Annett, A., van Beek, P., Garcia-Orellana, J., Hsieh, Y.-T., Masque, P., 2013. ²²⁶Ra
644 determination via the rate of ²²²Rn ingrowth with the Radium Delayed Coincidence Counter (RaDeCC).
645 *Limnology and Oceanography: Methods* 11, 594–603. <https://doi.org/10.4319/lom.2013.11.594>
- 646 Gonnee, M.E., Charette, M.A., Liu, Q., Herrera-Silveira, J.A., Morales-Ojeda, S.M., 2014. Trace element
647 geochemistry of groundwater in a karst subterranean estuary (Yucatan Peninsula, Mexico). *Geochimica et*
648 *Cosmochimica Acta* 132, 31–49. <https://doi.org/http://dx.doi.org/10.1016/j.gca.2014.01.037>
- 649 Guieu, C., Loÿe-Pilot, M.D., Benyahya, L., Dufour, A., 2010. Spatial variability of atmospheric fluxes of metals (Al,
650 Fe, Cd, Zn and Pb) and phosphorus over the whole Mediterranean from a one-year monitoring experiment:
651 Biogeochemical implications. *Marine Chemistry* 120, 164–178.
652 <https://doi.org/10.1016/j.marchem.2009.02.004>
- 653 Herut, B., Krom, M.D., Pan, G., Mortimer, R., 1999. Atmospheric input of nitrogen and phosphorus to the Southeast
654 Mediterranean: Sources, fluxes, and possible impact. *Limnology and Oceanography* 44, 1683–1692.
655 <https://doi.org/10.4319/lo.1999.44.7.1683>
- 656 Holmes, R.M., Aminot, A., K  rouel, R., Hooker, B.A., Peterson, B.J., 1999. A simple and precise method for
657 measuring ammonium in marine and freshwater ecosystems. *Canadian Journal of Fisheries and Aquatic*
658 *Sciences* 56, 1801–1808. <https://doi.org/10.1139/f99-128>
- 659 Kim, G., Kim, J.S., Hwang, D.W., 2011. Submarine groundwater discharge from oceanic islands standing in
660 oligotrophic oceans: Implications for global biological production and organic carbon fluxes. *Limnology and*
661 *Oceanography* 56, 673–682. <https://doi.org/10.4319/lo.2011.56.2.0673>
- 662 Krom, M.D., Kress, N., Brenner, S., Gordon, L.I., 1991. Phosphorus limitation of primary productivity in the eastern
663 Mediterranean Sea. *Limnology and Oceanography* 36, 424–432. <https://doi.org/10.4319/lo.1991.36.3.0424>
- 664 Lecher, A., Mackey, K., Lecher, A.L., Mackey, K.R.M., 2018. Synthesizing the Effects of Submarine Groundwater
665 Discharge on Marine Biota. *Hydrology* 5, 60. <https://doi.org/10.3390/hydrology5040060>

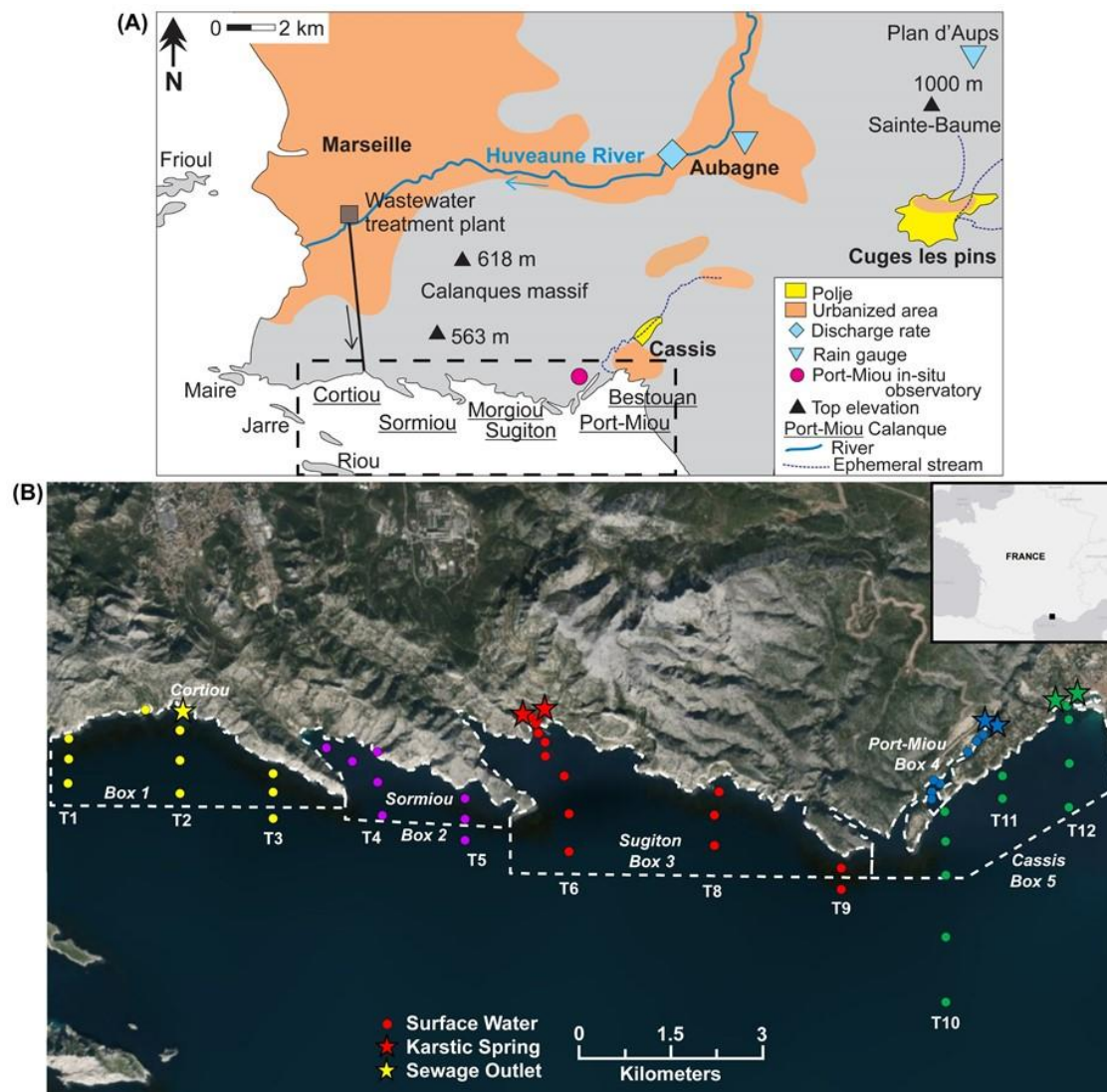
- 666 Luo, X., Jiao, J.J., Moore, W.S., Lee, C.M., 2014. Submarine groundwater discharge estimation in an urbanized
667 embayment in Hong Kong via short-lived radium isotopes and its implication of nutrient loadings and primary
668 production. *Marine Pollution Bulletin* 82, 144–154. <https://doi.org/10.1016/J.MARPOLBUL.2014.03.005>
- 669 Montiel, D., Dimova, N., Andreo, B., Prieto, J., García-Orellana, J., Rodellas, V., 2018. Assessing submarine
670 groundwater discharge (SGD) and nitrate fluxes in highly heterogeneous coastal karst aquifers: Challenges
671 and solutions. *Journal of Hydrology* 557, 222–242. <https://doi.org/10.1016/J.JHYDROL.2017.12.036>
- 672 Moore, W.S., Arnold, R., 1996. Measurement of Ra-223 and Ra-224 in coastal waters using a delayed coincidence
673 counter. *Journal of Geophysical Research-Oceans* 101, 1321–1329. <https://doi.org/10.1029/95JC03139>
- 674 Moore, W.S., Cai, P., 2013. Calibration of RaDeCC systems for 223Ra measurements. *Marine Chemistry* 156, 130–
675 137. <https://doi.org/10.1016/j.marchem.2013.03.002>
- 676 Moore, W.S., Reid, D.F., 1973. Extraction of radium from natural waters using manganese-impregnated acrylic
677 fibers. *Journal of Geophysical Research* 78, 8880–8886. <https://doi.org/10.1029/JC078i036p08880>
- 678 Morel, F.M.M., Price, N.M., 2003. The biogeochemical cycles of trace metals in the oceans. *Science (New York,
679 N.Y.)* 300, 944–7. <https://doi.org/10.1126/science.1083545>
- 680 Oursel, B., Garnier, C., Durrieu, G., Mounier, S., Omanović, D., Lucas, Y., 2013. Dynamics and fates of trace
681 metals chronically input in a Mediterranean coastal zone impacted by a large urban area. *Marine Pollution
682 Bulletin* 69, 137–149. <https://doi.org/10.1016/J.MARPOLBUL.2013.01.023>
- 683 Oursel, B., Garnier, C., Pairaud, I., Omanović, D., Durrieu, G., Syakti, A.D., le Poupon, C., Thouvenin, B., Lucas,
684 Y., 2014. Behaviour and fate of urban particles in coastal waters: Settling rate, size distribution and metals
685 contamination characterization. *Estuarine, Coastal and Shelf Science* 138, 14–26.
686 <https://doi.org/10.1016/J.ECSS.2013.12.002>
- 687 Pain, A.J., Martin, J.B., Young, C.R., Valle-Levinson, A., Mariño-Tapia, I., 2020. Carbon and phosphorus
688 processing in a carbonate karst aquifer and delivery to the coastal ocean. *Geochimica et Cosmochimica Acta*
689 269, 484–495. <https://doi.org/10.1016/J.GCA.2019.10.040>
- 690 Pavlidou, A., Papadopoulos, V.P., Hatzianestis, I., Simboura, N., Patiris, D., Tsabaris, C., 2014. Chemical inputs
691 from a karstic submarine groundwater discharge (SGD) into an oligotrophic Mediterranean coastal area.
692 *Science of The Total Environment* 488–489, 1–13. <https://doi.org/10.1016/J.SCITOTENV.2014.04.056>
- 693 Perez, T., Longet, D., Schembri, T., Rebouillon, P., Vacelet, J., 2005. Effects of 12 years' operation of a sewage
694 treatment plant on trace metal occurrence within a Mediterranean commercial sponge (*Spongia officinalis*,
695 *Demospongiae*). *Marine Pollution Bulletin* 50, 301–309. <https://doi.org/10.1016/J.MARPOLBUL.2004.11.001>
- 696 Price, R.M., Savabi, M.R., Jolicoeur, J.L., Roy, S., 2010. Adsorption and desorption of phosphate on limestone in
697 experiments simulating seawater intrusion. *Applied Geochemistry* 25, 1085–1091.
698 <https://doi.org/10.1016/J.APGEOCHEM.2010.04.013>
- 699 Pujo-Pay, M., Conan, P., Joux, F., Oriol, L., Naudin, J., Cauwet, G., 2006. Impact of phytoplankton and bacterial
700 production on nutrient and DOM uptake in the Rhône River plume (NW Mediterranean). *Marine Ecology
701 Progress Series* 315, 43–54. <https://doi.org/10.3354/meps315043>
- 702 Pujo-Pay, M., Conan, P., Oriol, L., Cornet-Barthaux, V., Falco, C., Ghiglione, J.-F., Goyet, C., Moutin, T., Prieur,
703 L., 2011. Integrated survey of elemental stoichiometry (C, N, P) from the western to eastern Mediterranean
704 Sea. *Biogeosciences* 8, 883–899. <https://doi.org/10.5194/bg-8-883-2011>
- 705 Pujo-Pay, M., Conan, P., Raimbault, P., 1997. Excretion of dissolved organic nitrogen by phytoplankton assessed by
706 wet oxidation and 15N tracer procedures. *Marine Ecology Progress Series* 153, 99–111.
707 <https://doi.org/10.3354/meps153099>
- 708 Pujo-Pay, M., Raimbault, P., 1994. Improvement of the wet-oxidation procedure for simultaneous determination of
709 particulate organic nitrogen and phosphorus collected on filters 105, 203–207.
- 710 Rodellas, V., Garcia-Orellana, J., Masque, P., Feldman, M., Weinstein, Y., 2015. Submarine groundwater discharge
711 as a major source of nutrients to the Mediterranean Sea. *Proceedings of the National Academy of Sciences of
712 the United States of America* 112, 3926–3930. <https://doi.org/10.1073/pnas.1419049112>

- 713 Rodellas, V., Garcia-Orellana, J., Tovar-Sánchez, A., Basterretxea, G., López-García, J.M., Sánchez-Quiles, D.,
714 Garcia-Solsona, E., Masqué, P., 2014. Submarine groundwater discharge as a source of nutrients and trace
715 metals in a Mediterranean bay (Palma Beach, Balearic Islands). *Marine Chemistry* 160, 56–66.
716 <https://doi.org/10.1016/J.MARCHEM.2014.01.007>
- 717 Rodellas, V., Stieglitz, T.C., Andrisoa, A., Cook, P.G., Raimbault, P., Tamborski, J.J., van Beek, P., Radakovitch,
718 O., 2018. Groundwater-driven nutrient inputs to coastal lagoons: The relevance of lagoon water recirculation
719 as a conveyor of dissolved nutrients. *Science of the Total Environment* 642.
720 <https://doi.org/10.1016/j.scitotenv.2018.06.095>
- 721 Romey, C., Rochette, P., Vella, C., Arfib, B., Andrieu-Ponel, V., Braucher, R., Champollion, C., Douchet, M.,
722 Dussouillez, P., Hermitte, D., Mattioli, E., Parisot, J.-C., Schwenninger, J.-L., 2014. Geophysical and
723 geomorphological investigations of a Quaternary karstic paleolake and its underground marine connection in
724 Cassis (Bestouan, Cassis, SE France). *Geomorphology* 214, 402–415.
725 <https://doi.org/10.1016/J.GEOMORPH.2014.02.021>
- 726 Savriama, Y., Stige, L.C., Gerber, S., Pérez, T., Alibert, P., David, B., 2015. Impact of sewage pollution on two
727 species of sea urchins in the Mediterranean Sea (Cortiou, France): Radial asymmetry as a bioindicator of
728 stress. *Ecological Indicators* 54, 39–47. <https://doi.org/10.1016/J.ECOLIND.2015.02.004>
- 729 Slomp, C.P., van Cappellen, P., 2004. Nutrient inputs to the coastal ocean through submarine groundwater
730 discharge: controls and potential impact. *Journal of Hydrology* 295, 64–86.
731 <https://doi.org/10.1016/j.jhydrol.2004.02.018>
- 732 Sugimura, Y., Suzuki, Y., 1988. A high-temperature catalytic oxidation method for the determination of non-volatile
733 dissolved organic carbon in seawater by direct injection of a liquid sample. *Marine Chemistry* 24, 105–131.
734 [https://doi.org/10.1016/0304-4203\(88\)90043-6](https://doi.org/10.1016/0304-4203(88)90043-6)
- 735 Sun, Y., Torgersen, T., 1998. The effects of water content and Mn-fiber surface conditions on 224Ra measurement
736 by 220Rn emanation. *Marine Chemistry* 62, 299–306. [https://doi.org/10.1016/S0304-4203\(98\)00019-X](https://doi.org/10.1016/S0304-4203(98)00019-X)
- 737 Tamborski, J., Beek, P., Rodellas, V., Monnin, C., Bergsma, E., Stieglitz, T., Heilbrun, C., Cochran, J.K.,
738 Charbonnier, C., Anschutz, P., Bejannin, S., Beck, A., 2019. Temporal variability of lagoon–sea water
739 exchange and seawater circulation through a Mediterranean barrier beach. *Limnology and Oceanography*
740 *Ino.11169*. <https://doi.org/10.1002/Ino.11169>
- 741 Tamborski, J., Bejannin, S., Garcia-Orellana, J., Souhaut, M., Charbonnier, C., Anschutz, P., Pujo-Pay, M., Conan,
742 P., Crispi, O., Monnin, C., Stieglitz, T., Rodellas, V., Andrisoa, A., Claude, C., van Beek, P., 2018. A
743 comparison between water circulation and terrestrially-driven dissolved silica fluxes to the Mediterranean Sea
744 traced using radium isotopes. *Geochimica et Cosmochimica Acta* 238, 496–515.
745 <https://doi.org/10.1016/J.GCA.2018.07.022>
- 746 Tovar-Sanchez, A., Basterretxea, G., Rodellas, V., Sanchez-Quiles, D., Garcia-Orellana, J., Masque, P., Jordi, A.,
747 Lopez, J.M., Garcia-Solsona, E., 2014. Contribution of Groundwater Discharge to the Coastal Dissolved
748 Nutrients and Trace Metal Concentrations in Majorca Island: Karstic vs Detrital Systems. *Environmental*
749 *Science & Technology* 48, 11819–11827. <https://doi.org/10.1021/es502958t>
- 750 Trezzi, G., Garcia-Orellana, J., Rodellas, V., Santos-Echeandia, J., Tovar-Sánchez, A., Garcia-Solsona, E., Masqué,
751 P., 2016. Submarine groundwater discharge: A significant source of dissolved trace metals to the North
752 Western Mediterranean Sea. *Marine Chemistry* 186, 90–100. <https://doi.org/10.1016/j.marchem.2016.08.004>
- 753 Twining, B.S., Baines, S.B., 2013. The Trace Metal Composition of Marine Phytoplankton. *Annual Review of*
754 *Marine Science* 5, 191–215. <https://doi.org/10.1146/annurev-marine-121211-172322>
- 755 van Wambeke, F., Ghiglione, J.-F., Nedoma, J., Mével, G., Raimbault, P., 2009. Bottom up effects on
756 bacterioplankton growth and composition during summer-autumn transition in the open NW Mediterranean
757 Sea. *Biogeosciences* 6, 705–720. <https://doi.org/10.5194/bg-6-705-2009>
- 758 Wang, X., Li, H., Zheng, C., Yang, J., Zhang, Y., Zhang, M., Qi, Z., Xiao, K., Zhang, X., 2018. Submarine
759 groundwater discharge as an important nutrient source influencing nutrient structure in coastal water of Daya
760 Bay, China. *Geochimica et Cosmochimica Acta* 225, 52–65. <https://doi.org/10.1016/J.GCA.2018.01.029>

761 Windom, H.L., Moore, W.S., Niencheski, L.F.H., Jahnke, R.A., 2006. Submarine groundwater discharge: A large,
762 previously unrecognized source of dissolved iron to the South Atlantic Ocean. *Marine Chemistry* 102, 252–
763 266. <https://doi.org/10.1016/J.MARCHEM.2006.06.016>

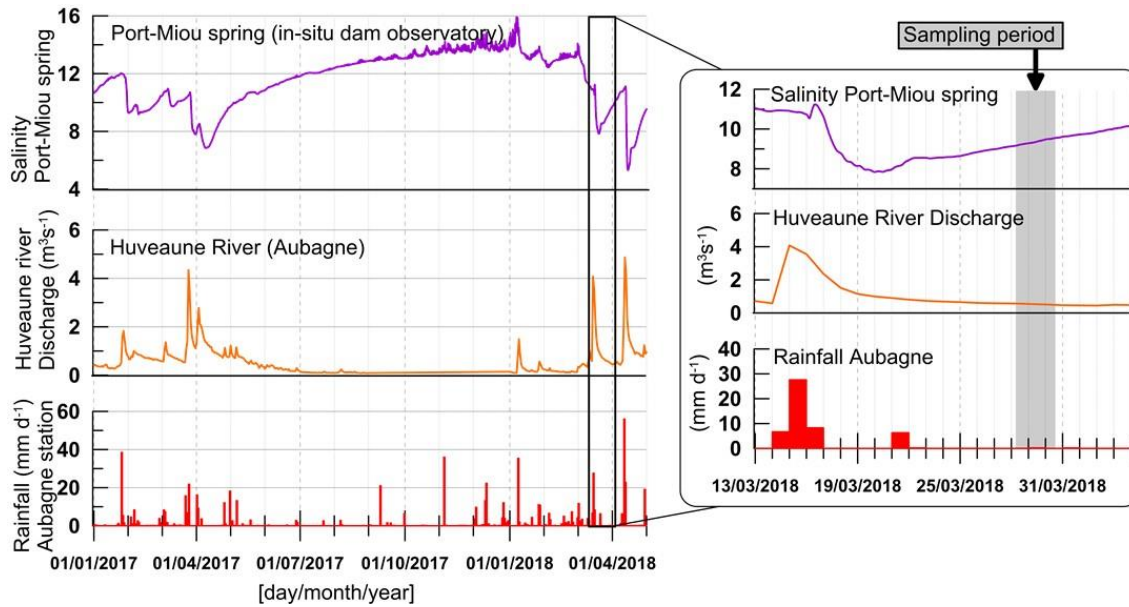
764

765



766

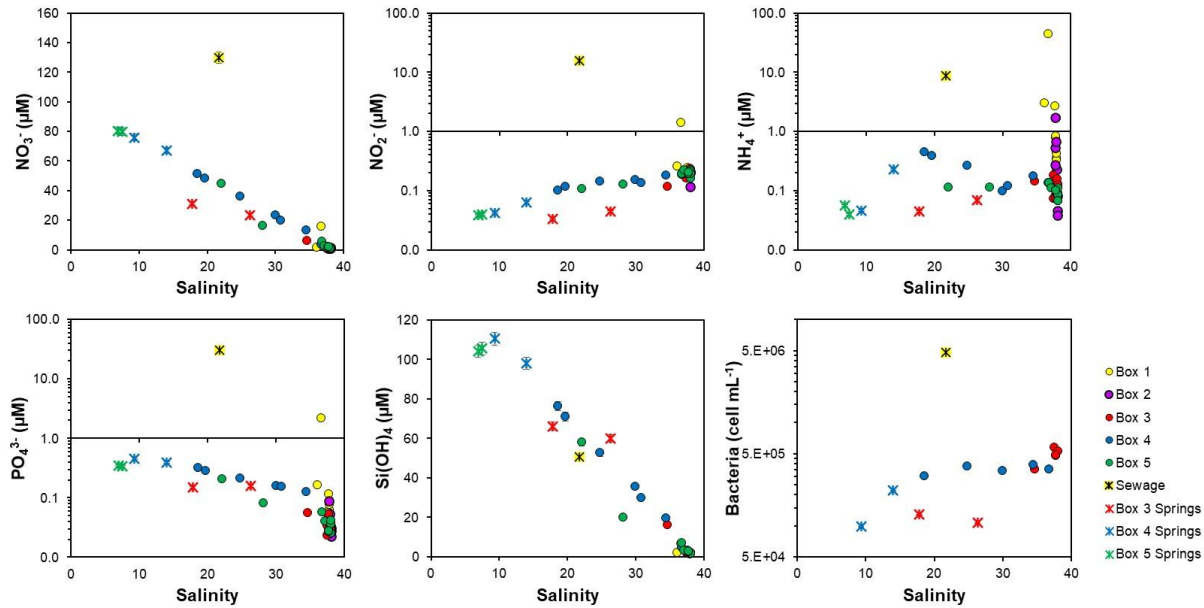
767 **Figure 1.** The Calanques of Marseille-Cassis (A), situated along the French Mediterranean coastline (B, inset black
 768 square). The black dashed rectangle in (A) corresponds to the location of subset panel (B). Surface water (circle),
 769 karstic groundwater (red, blue and green stars) and sewage effluent (yellow star) sampling stations are shown for the
 770 period 27th – 29th March, 2018. Transect labels (T1 – T12) are listed below each respective transect; note there is no
 771 T7.



772

773 **Figure 2.** Port-Miou groundwater spring salinity (top) measured at the Port-Miou *in-situ* observatory, Huveaune River
 774 daily discharge (middle) measured at the Aubagne station upstream of Marseille and daily rainfall (bottom) from the
 775 nearby Aubagne station (Lat: 43.30667, Lon: 5.60000, z = 130 m; Figure 1A). Left panel: Long time-series (17
 776 months). Right panel: Time-series of the two weeks preceding the sampling period (salinity recorded at 15-minute
 777 time-steps, average daily discharge); the sampling period of this study is indicated by a light-gray rectangle.

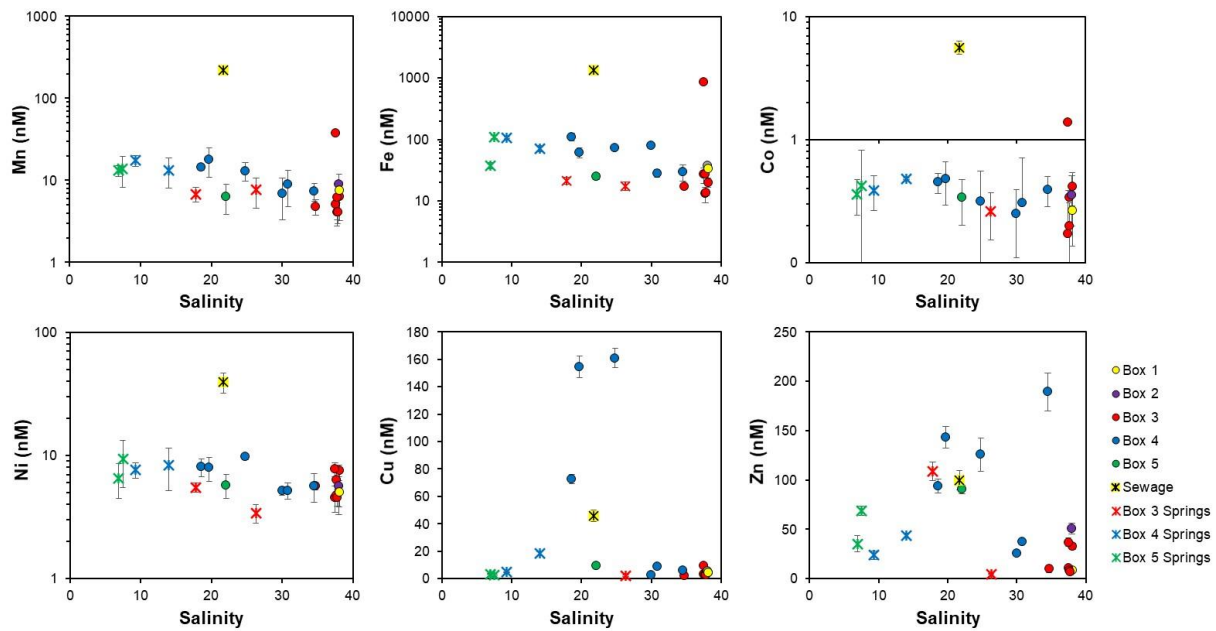
778



779

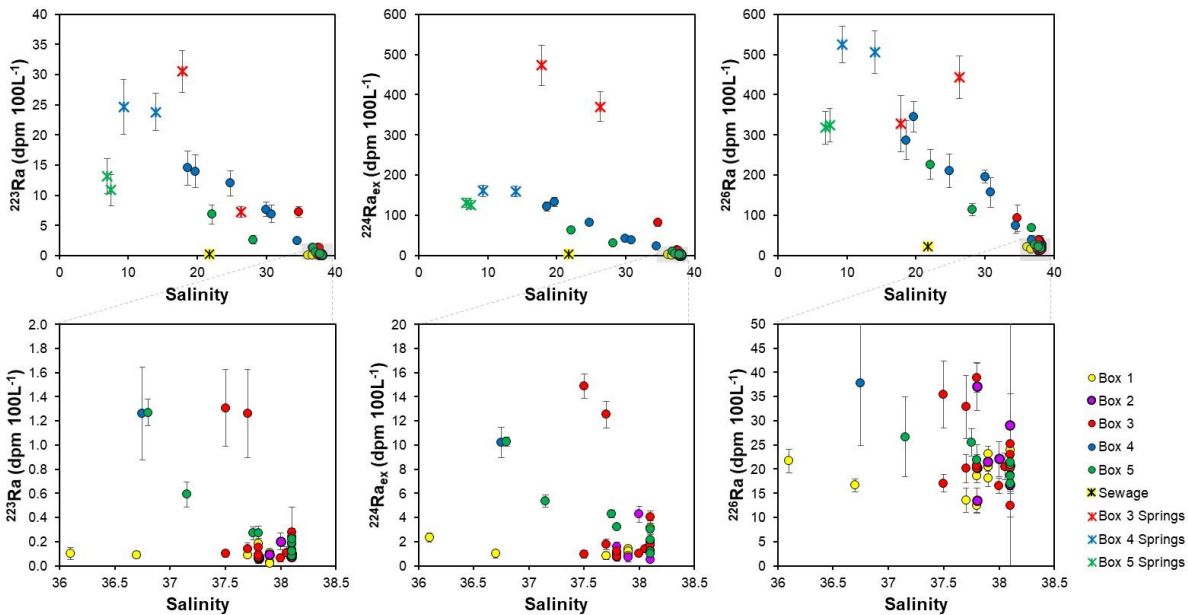
780 **Figure 3.** Major nutrient concentration and bacterial biomass versus salinity for coastal surface waters (circles), karstic
 781 springs (crosses) and water samples collected at the outlet of the Cortiou sewage outlet (yellow cross) on 27th – 29th
 782 March, 2018. Note the y-axes for NO₂⁻, NH₄⁺, PO₄³⁻ and bacterial biomass are log-scale. Only select samples were
 783 analyzed for bacterial biomass.

784



785

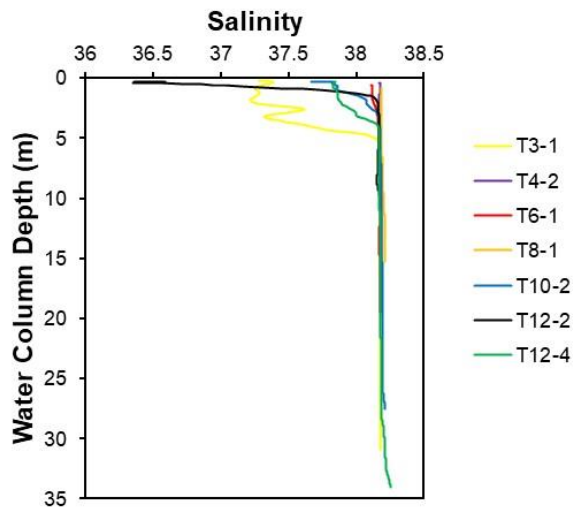
786 **Figure 4.** Trace element concentration versus salinity for select coastal surface waters (circles), karstic springs
 787 (crosses) and water samples collected at the outlet of the Cortiou sewage outlet (yellow cross) on 27th – 29th March,
 788 2018. Note that the y-axes for Mn, Fe, Co and Ni are log-scale.



789

790 **Figure 5.** Ra isotope activity versus salinity for coastal surface waters (circles), karstic springs (crosses) and water
 791 samples collected at the outlet of the Cortiou sewage outlet (yellow cross) on 27th – 29th March, 2018. The lower
 792 panels represent the area of the gray rectangle of the above panel.

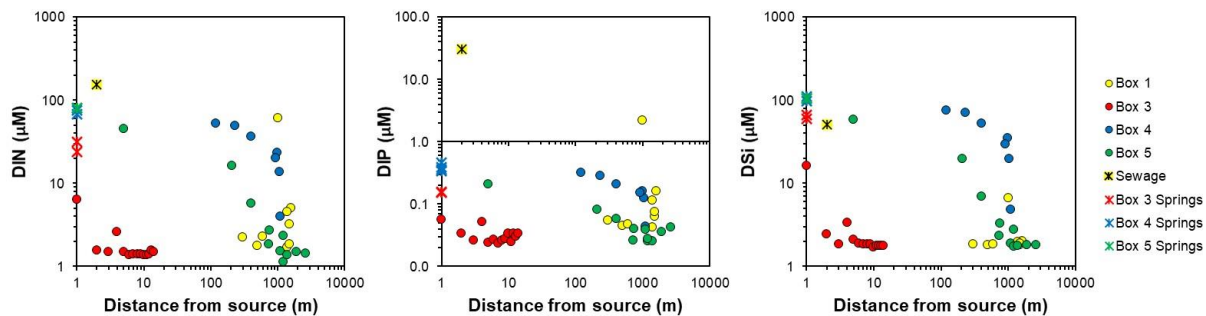
793



794

795 **Figure 6.** Select salinity profiles of the Calanques of Marseille-Cassis. Transect locations are shown on Figure 1; the
 796 second number corresponds to the offshore sample position for each respective transect. T3-1 = box 1, T4-2 = box 2,
 797 T6-1 & T8-1 = box 3, T10-2 = box 4/5 boundary, T12-2 & T12-4 = box 5.

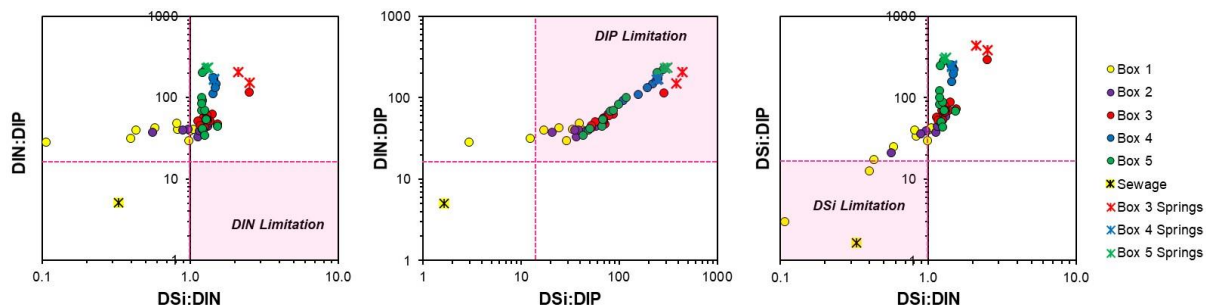
798



799

800 **Figure 7.** Surface water nutrient concentrations as a function of distance from a known point-source (sewage outlet
 801 or karstic spring). Only select stations are shown, in which the surface water sampling locations distance to the nearest
 802 known point-source could be well-defined; as a result, no stations are included for Box 2. Distances were measured
 803 using high resolution visible light imagery in Google Earth and assume a 20% measurement uncertainty. $DIN = NO_2^-$
 804 $+ NO_3^- + NH_4^+$; $DIP = PO_4^{3-}$; $DSi = Si(OH)_4$.

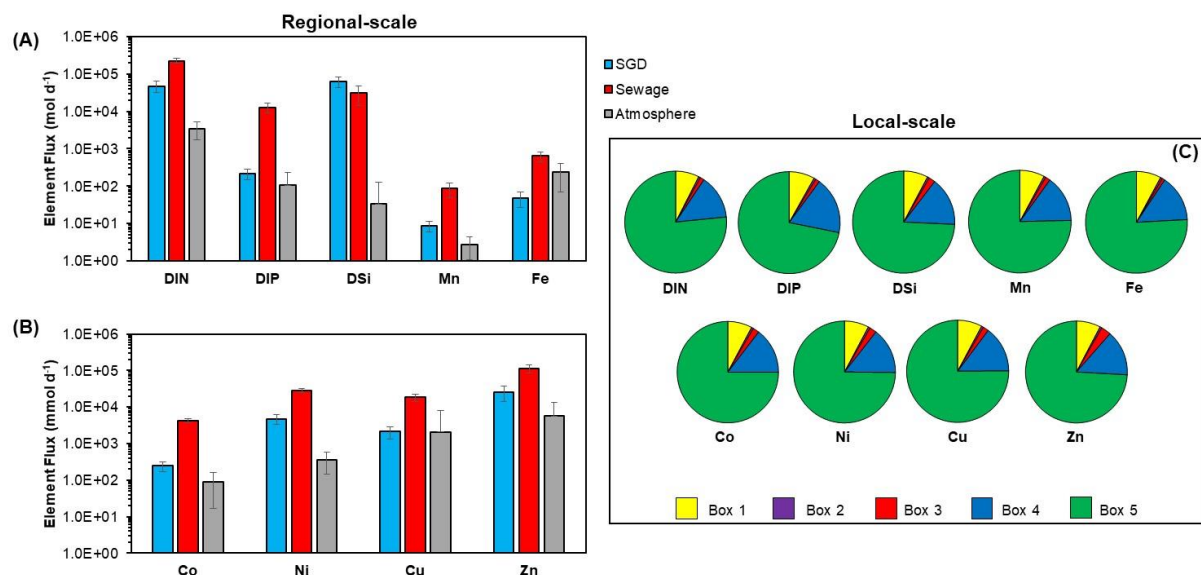
805



806

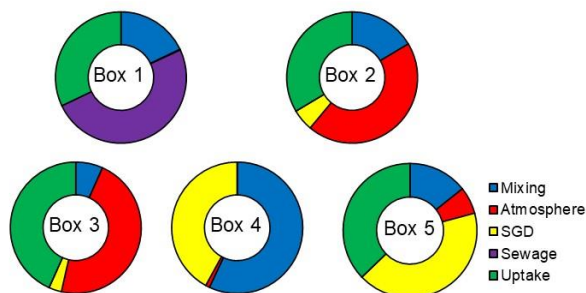
807 **Figure 8.** Relationships between stoichiometric ratios of DIN:DIP, DSi:DIN and DSi:DIP. Nutrient limitation is
 808 indicated by a shaded pink box for DIN (A), DIP (B) and DSi (C). $DIN = NO_2^- + NO_3^- + NH_4^+$; $DIP = PO_4^{3-}$; $DSi =$
 809 $Si(OH)_4$.

810



811
 812 **Figure 9.** Comparison between chemical element fluxes from SGD (during 27th – 29th March, 2018), sewage effluent
 813 and atmospheric deposition to the entire shoreline of the Calanques of Marseille-Cassis. Note that regional fluxes in
 814 the upper panel (A) are reported in mol d⁻¹ and in the lower panel (B) fluxes are reported in mmol d⁻¹. Pie charts (C)
 815 represent SGD-driven solute fluxes to each coastal box (local-scale). DIN = NO₂⁻ + NO₃⁻ + NH₄⁺; DIP = PO₄³⁻; DSi =
 816 Si(OH)₄.

817



818
 819 **Figure 10.** Summary of the coastal surface water DIP (PO₄³⁻) budget during the study period, expressed as a
 820 percentage (Eq. 3) and arranged by box. Note that atmospheric inputs to Box 1 < 1%.

821